ACS APPLIED MATERIALS & INTERFACES

Research Article

www.acsami.org

Electrolytically Exfoliated Graphene-Loaded Flame-Made Ni-Doped SnO_2 Composite Film for Acetone Sensing

Suparat Singkammo,[†] Anurat Wisitsoraat,[‡] Chakrit Sriprachuabwong,[‡] Adisorn Tuantranont,[‡] Sukon Phanichphant,[§] and Chaikarn Liewhiran*[,†,§]

[†]Department of Physics and Materials Science, Faculty of Science, Chiang Mai University, Chiang Mai 50202, Thailand

[‡]Nanoelectronics and MEMS Laboratory, National Electronics and Computer Technology Center, National Science and Technology Development Agency, Klong Luang, Pathumthani 12120, Thailand

[§]Materials Science Research Center, Faculty of Science, Chiang Mai University, Chiang Mai 50202, Thailand

ABSTRACT: In this work, flame-spray-made SnO_2 nanoparticles are systematically studied by doping with 0.1−2 wt % nickel (Ni) and loading with 0.1−5 wt % electrolytically exfoliated graphene for acetone-sensing applications. The sensing films (~12−18 μm in thickness) were prepared by a spin-coating technique on Au/Al_2O_3 substrates and evaluated for acetone-sensing performances at operating temperatures ranging from 150 to 350 °C in dry air. Characterizations by X-ray diffraction, transmission/scanning electron microscopy, Brunauer−Emmett−Teller analysis, X-ray photoelectron spectroscopy and Raman spectroscopy demonstrated that Ni-doped SnO_2 nanostructures had a spheriodal morphology with a polycrystalline tetragonal SnO_2 phase, and Ni was confirmed to form a solid solution with SnO_2 lattice while graphene in the sensing film after annealing and testing still retained its high-quality nonoxidized form. Gas-sensing results showed that SnO_2 sensing film with 0.1 wt % Ni-doping concentration exhibited an optimal response of 54.2 and a short response time of ~13 s toward 200 ppm acetone at an optimal operating temperature of 350 °C. The additional loading of graphene at 5 wt % into 0.1 wt % Ni-doped SnO_2 led to a drastic response enhancement to 169.7 with a very short response time of ~5.4 s at 200 ppm acetone and 350 °C. The superior gas sensing performances of Ni-doped SnO_2 nanoparticles loaded with graphene may be attributed to the large specific surface area of the composite structure, specifically the high interaction rate between acetone vapor and graphene−Ni-doped SnO_2 nanoparticles interfaces and high electronic conductivity of graphene. Therefore, the 5 wt % graphene loaded 0.1 wt % Ni-doped SnO_2 sensor is a promising candidate for fast, sensitive and selective detection of acetone.

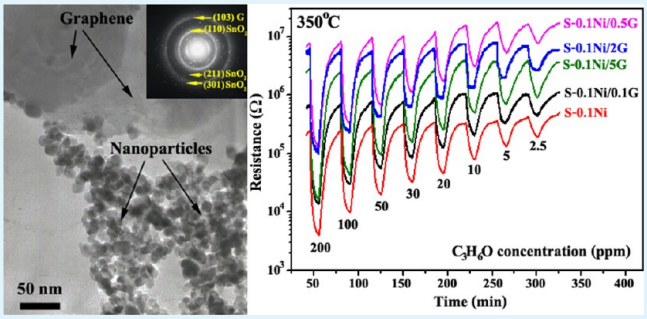

KEYWORDS: *flame spray pyrolysis, acetone, SnO_2, Ni-doping, graphene, gas sensor*

1. INTRODUCTION

Volatile organic compounds (VOCs) are widely used active substances in various chemical-related industries. Due to their volatility and toxicity, they are becoming important environmentally hazardous pollutants that pose a serious threat to human health. VOCs the enter the human body through breathing will transport via the bloodstream to many organs and adversely affect brain, nervous, endocrine and skin systems, even at low concentrations.[1−4] Acetone (C_3H_6O), a widely used VOC in industries and laboratories, is toxic to various organ systems and is a selective breath marker for type-1 diabetes.[5] The acetone concentration in the breath of a healthy individual should be below 0.9 ppm and the concentration of more than 1.8 ppm could indicate ketosis (high ketone level in blood) of insulin-dependent diabetes. Thus, highly sensitive and selective sensors for acetone detection are required for the rapid assessment of diabetes and related diseases.[5,6] Detections of VOCs at low concentrations have typically been conducted based on expensive analytical instruments such as gas chromatography devices, which are normally only available in laboratories. VOC sensors on the basis of semiconductor metal oxide nanomaterials are promising alternatives for rapid estimation of VOCs in the field due to its low cost, high sensitivity and satisfactory selectivity. However, the performances of semiconductor gas sensors must be further improved to meet various requirements, particularly sensitivity and selectivity toward particular VOCs.

Metal oxide semiconductors as gas-sensing materials have been widely for various types of gases due to their stable chemical transduction properties, which can reversibly convert chemical interactions on a surface to change the electrical conductivity.[7−15] Particularly, tin dioxide (SnO_2) is the best-understood and commercially used semiconducting metal oxide material due to numerous advantages including low cost, high

Received: October 6, 2014
Accepted: January 20, 2015
Published: January 20, 2015

DOI: 10.1021/acsami.5b00161
ACS Appl. Mater. Interfaces 2015, 7, 3077−3092

Table 1. Summary of Gas-Sensing Performances toward VOCs of Ni-Doped and Graphene-Loaded SnO_2 Gas Sensors Prepared by Various Synthetic Methods

authors	sensing materials	method	gas concentration	sensing performance
Bagal et al.[21]	SnO_2 2 wt % Ni/SnO_2 4 wt % Ce/SnO_2 2 wt % Ni−4 wt % Ce codoped SnO_2	coprecipitation	acetone 0.2−500 ppm 300 °C	31% 38% 60% 92% S = 500 ppm t_{res} = 23 s, t_{rec} = 1 min
Chen et al.[22]	Ni-doped SnO_2 hollow spheres	hydrothermal	ethanol 59−100 ppm 350 °C	S = 59, 100 ppm t_{res} = 2 s, t_{rec} = 15 s
Liu et al.[23]	Ni-doped SnO_2 hollow spheres	carbon microsphere template	*n*-butanol ethanol 2−50 ppm 300 °C	∼28, 50 ppm ∼15, 50 ppm selectivity = *n*-butanol
Lee et al.[24]	3 wt % Ni-doped SnO_2 thick film	powder impregnation to dichloromethane (DCH)	ethanol 0.1−0.8 ppm 350 °C	∼50%, 0.5 ppm
Cheng et al.[25]	Ni-doped SnO_2 hollow nanofibers	electrospinning	acetone 2−1000 ppm 340 °C	S = 265, 1000 ppm t_{res} = 7 s, t_{rec} = 30 s
Meng et al.[28]	SnO_2/graphene nanocomposite	wet chemical	benzene, ethanol toluene, methanol chlorobenzene *n*-propanol 5−100 ppb 210 °C	S = 94.3%, 100 ppb benzene selectivity = benzene
Lin et al.[29]	SnO_2/graphene composite	hydrothermal	NH_3 10−50 ppm 15−45 °C	S = 15.9%, 50 ppm, 45 °C <1 min
Zhang et al.[30]	SnO_2 nanoparticles /reduced graphene oxide	hydrothermal	NO_2 0.5−5 ppm 50 °C	S = 3.31, 5 ppm t_{res} = 135 s, t_{rec} = 200 s
Chang et al.[31]	SnO_2/reduced graphene oxide composites	hydrothermal	ethanol H_2S 0.56−1.68 ppm, 300 °C	S = 22, 1.16 ppm S = 11, 1.16 ppm t_{res} = 22 s, t_{rec} = 36 s selectivity = ethanol
present work	0−2 wt % Ni/SnO_2 0.1 wt %Ni/SnO_2 /0.1−5wt % graphene (G)	FSP (powders) impregnation (composite) spin-coating (sensors)	acetone, 2.5−200 ppm ethanol, 2.5−200 ppm H_2, CH_4, 5−400 ppm H_2S, 0.2−10 ppm NO_2, 0.1−5 ppm 150−350 °C	acetone, 200 ppm 0.1 wt % Ni/SnO_2 S = 54.4, t_{res} = 13 s, t_{rec} = 3 min 0.1 wt % Ni/SnO_2/5 wt % G S = 169.7, t_{res} = 5.4 s, t_{rec} = 2.5 min selectivity = acetone

ACS Appl. Mater. Interfaces 2015, 7, 3077−3092
DOI: 10.1021/acsami.5b00161

sensitivity to various reducing/oxidizing gases and compatibility with microfabrication processes.[7−9] However, its gas-sensing performances still need to be further improved for sensitive and specific detection toward particular gases such as acetone. These goals may be achieved by employing porous SnO_2 nanostructures possessing peculiar properties of large specific surface area and incorporating some effective additive materials. Transition metals such as Pt,[16] Pd,[17] Co,[18] Fe[19] and Ni,[20] as well as their oxides, are widely studied additives for SnO_2 gas sensors due to their effective catalytic properties. In particular, Ni and NiO *p*-type catalysts have been employed to improve sensing performances of SnO_2 sensors toward VOCs. Gas-sensing properties of Ni-doped or NiO-loaded SnO_2 sensors prepared by several synthetic methods toward various VOCs are summarized in Table 1.

First, resistance-change response of nanocrystalline SnO_2 thick film synthesized by a coprecipitation route was found to improve from 1.44 to 1.61, 2.5, and 12.5 toward 500 ppm acetone at 300 °C by doping with 2 wt % Ni, 4 wt % Ce and 2 wt % Ni−4 wt % Ce, respectively.[21] Additionally, porous Ni-doped SnO_2 hollow spheres synthesized by a hydrothermal strategy showed a high response of ∼59 to 100 ppm ethanol with a short response time of a few seconds and a low detection limit of 1 ppm.[22] Likewise, Ni-doped SnO_2 hollow spheres prepared by a carbon microsphere-template technique displayed good selectivity toward *n*-butanol against ethanol and acetone with relative responses at 50 ppm and 300 °C of ∼28, 15 and 4, respectively, whereas the undoped sensor exhibited poor responses and selectivity to all gases.[23] Moreover, Ni/SnO_2 thick film synthesized by 3 wt % NiO powder impregnation revealed a good response of ∼50% to 0.5 ppm dichloromethane (DCH) at 350 °C whereas undoped SnO_2 exhibited a very low response value.[24] Moreover, 5 at. % Ni-doped SnO_2 hollow porous nanofibers fabricated by an electrospinning technique exhibited a high response of 265.2 to 1000 ppm acetone at 340 °C with short response/recovery times (7 s/30 s) and good selectivity against other VOCs including methanol, ethanol and chloroform.[25]

Graphene, a novel 2D nanocarbon material, has recently been widely studied as a new additive material for gas-sensing due to its large specific surface area, strong gas adsorption capacity, high carrier mobility and excellent electronic conductivity.[26−33] In particular, graphene has been incorporated into SnO_2-based materials and the incorporation can considerably enhance sensing responses toward various gases, especially VOCs, as illustrated in Table 1.[28−31] For instance, a SnO_2nanoparticle/graphene nanocomposite prepared by a simple wet chemical method provided high responses to VOCs, specifically benzene (conductivity change of 94.3% at 100 ppb and 210 °C), whereas SnO_2 nanoparticles gave negligible benzene responses at ppb-level concentrations.[29] Similarly, a graphene/SnO_2−nanoparticle composite synthesized by a hydrothermal route exhibited a fair resistance-change response of 15.9% to 50 ppm NH_3 with a short response time (<1 min) at low and room-temperatures (15−45 °C) whereas pristine SnO_2 sensors had no NH_3 response at room temperature.[28] Likewise, the reduced-graphene-oxide (RGO)/SnO_2 composite made by another hydrothermal method showed a high response of 3.31 to 5 ppm NO_2 at a low temperature of 50 °C.[30] In addition, the RGO/SnO_2 composite prepared by a similar hydrothermal process displayed high ethanol and H_2S responses of 22 and 11 at 1.16 ppm and 300 °C with short response/recovery times.[31] Therefore, nickel doping as well as graphene incorporation have been demonstrated to be effective means to enhance gas-sensing performances toward VOCs, and their combination should be a highly promising route to high-performance VOC sensors. However, there has been no report of Ni-doped SnO_2/graphene composite for VOCs detection.

In this work, Ni-doped SnO_2 nanoparticle/graphene composites are developed for the first time by flame spray pyrolysis (FSP) and paste mixing with graphene powder synthesized by electrolytic exfoliation. FSP is an attractive nanopowder production strategy that can produce various metal-doped/loaded metal oxide nanoparticles with large specific surface area in a single high-temperature step whereas electrolytic exfoliation is also a relatively new single-step graphene synthesis method. Recently, a variety of unloaded and metal-loaded/doped metal oxide nanoparticles have been successfully manufactured by FSP and demonstrated for detection of various kinds of gases by our group.[8,11,17] Nevertheless, FSP-made SnO_2 nanoparticles have not been doped with nickel and incorporated with graphene for acetone sensing. Thus, the effect of nickel and graphene concentrations in the hybrid material on gas-sensing performances will be systematically studied and optimized for selective detection of acetone.

2. MATERIALS AND METHODS

2.1. Synthesis and Characterization of Metal Oxide and Graphene Nanopowders. Undoped SnO_2 and 0.1−2 wt %Ni-doped SnO_2 nanoparticles were synthesized by FSP technique based on the procedure reported previously.[11,17] Briefly, the precursor solution (0.5 M) comprising tin(II) 2-ethylhexanoate (Aldrich, 95%) and nickel acetylacetonate (Aldrich, 99%) in the solvent mixture (80/20 vol %) of xylene (Carlo Erba, 98.5%)/acetonitrile (Lab-scan, 99.7%) was sprayed through O_2 dispersion into a premixed CH_4/O_2 (5/5) flame. Precursor droplets were vaporized and combusted to form nanoparticles via nucleation, condensation, coagulation, coalescence and Ni-doping on a SnO_2 support. The FSP-made unloaded SnO_2 nanopowder was labeled as P-0 whereas SnO_2 nanopowders doped with 0.1, 0.2, 0.5, 1 and 2 wt % Ni were designated as P-0.1Ni, P-0.2Ni, P-0.5Ni, P-1Ni and P-2Ni, respectively.

Graphene (G) was produced from graphite by the electrolytic exfoliation process reported earlier.[32,33] Shortly, a direct potential of 8 V was applied between two graphite rods (1/4 in. dia, Electron Microscopy Science) immersed in 0.1 wt % poly(styrenesulfonate) (PSS) (Sigma-Aldrich) electrolyte solution for 7 days to yield high-density graphene dispersion. The graphene powder was then obtained by centrifugation at 1200 rpm to separate large graphite agglomerates, washing in distilled water and drying at 80 °C.

The phases of powder were analyzed by X-ray diffraction (XRD) (Phillips X'Pert) using Cu Kα radiation (20 kV, 20 mA) with a scanning speed of 5°/min. The morphologies of nanoparticles were examined by transmission electron microscopy (TEM: JSM-2010, JEOL). The specific surface area of nanoparticles was measured by nitrogen absorption with Brunauer−Emmett−Teller (BET) analysis (Micromeritics Tristar 3000). All samples were degassed at 120 °C for 2 h prior to BET measurement. The effective particle diameter was calculated from $d_{BET} = 6/SSA_{BET} \times \rho_{samples}$,[8,17,34] where SSA_{BET} and $\rho_{samples}$ was the specific surface area (m^2/g) and the average density of graphene−Ni-doped SnO_2 composite (g/m^3), respectively. In addition, the chemical fingerprint and vibration modes of material were verified by Raman spectroscopy (Jobinyvon horiba, T-64000). Moreover, X-ray photoelectron spectroscopy (XPS) was performed to analyze the chemical states and elemental compositions of nanoparticles.

2.2. Sensing Film Fabrication and Characterizations. To form a paste for spin-coating of a sensing film, as-prepared FSP-made 0−2 wt % Ni-doped SnO_2 and graphene-loaded (0.1−5 wt % G)

DOI: 10.1021/acsami.5b00161
ACS Appl. Mater. Interfaces 2015, 7, 3077−3092

nanopowders were thoroughly mixed and ground with the binder solution comprising ethyl cellulose (Fluka, 30−70 mPa·s) and α-terpineol (Aldrich, 90%). The produced paste was spin-coated on Al_2O_3 substrates (0.4 × 0.5 × 0.1 cm) equipped with Au interdigitated electrodes. The resulting sensing films on substrates were baked at 150 °C for 1 h and then subsequently annealed at 450 °C for 2 h in an oven for binder removal. The sensors fabricated from P-0 and P-0.1Ni to P-2Ni powder samples were designated as S-0 and S-0.1Ni to S-2Ni, respectively, while powders and films with additional graphene loadings at 0.1, 0.5, 2 and 5 wt % would have additional postlabel of /0.1G, /0.5G, /2G and /5G, respectively.

The phase and crystallinity of Ni-doped SnO_2 sensing films were analyzed by glancing incident X-ray diffraction (GI-XRD) [Rigaku, TTRAX III] using Cu Kα radiation (30 kV, 15 mA) with the detector scanning speed of 3° per minute. The surface morphologies and cross-sectional structures of Ni-doped SnO_2 and Ni-doped SnO_2/graphene composite films after annealing and sensing test were examined by field emission-scanning electron microscopy (FE-SEM: JSM-6335F, JEOL). Moreover, the oxidation state and chemical composition after annealing and sensing test were evaluated by X-ray photoelectron spectroscopy (XPS) using an AXIS Ultra DLD-X-ray photoelectron spectrometer and a monochromatic Al Kα X-ray excitation source.

2.3. Gas-Sensing Measurement. The gas-sensing performances of sensing films were characterized for acetone sensing in the concentration range of 2.5−200 ppm at operating temperatures ranging from 150 to 350 °C by the standard flow-through technique. A constant flux of synthetic air as the gas carrier was flowed to mix with the desired concentration of pollutants dispersed in synthetic air with the total gas flow rate of 2 L/min. All gas sources were 2,000 ppm calibrated gas balanced in synthetic air and gas dilution was precisely manipulated by mass flow controllers (Brook Instruement Inc.). The sensor was exposed to a gas sample for ∼10 min at each gas concentration, and the pure synthetic air flow was then resumed for 25 min. The gas-sensing data were then analyzed in terms of sensor response, response time and recovery time. The sensor response (S) is defined as the resistance ratio R_a/R_g,[8,11,17,34] where R_a is the resistance in dry air and R_g is the resistance after exposure to a reducing gas. The sensor response definition is reversed for an oxidizing gas. The response time (t_{res}) is defined as the time required until 90% of the response signal is reached while the recovery time (t_{rec}) denotes the time needed until 90% of the original baseline signal is recovered.

3. RESULTS AND DISCUSSION

3.1. Properties of Nanoparticles and Sensing Films. XRD patterns of FSP-made undoped SnO_2 (P-0) and 0.1−2 wt % Ni-doped SnO_2 (P-0.1Ni to P-2Ni) nanopowders are shown Figure 1a. It is seen that all samples exhibit high crystallinity with sharp XRD peaks, which are well matched with the cassiterite-tetragonal phase of SnO_2 (JCPDS file No. 41-1445). In addition, undoped and Ni-doped SnO_2 nanopowders display similar diffraction patterns with (1 1 0), (1 0 1), (2 0 0) and (2 1 1) preferred crystallographic orientations and a high Ni doping level (1−2 wt %) noticeably causes peak broadening at high index planes, suggesting an increasing level of nanoscale defects. However, peaks of Ni phase cannot be seen in these patterns due possibly to the formation of Ni−SnO_2 solid solution or the absence of large crystalline NiO_x particles (>10 nm). Figure 1b shows XRD patterns of graphene and FSP-made 0.1 wt % Ni-doped SnO_2 (P-0.1Ni) nanoparticles with various graphene loading concentrations ranging from 0 to 5 wt % after annealing and sensing test. It is evident that electrolytically exfoliated graphene exhibits crystalline graphite-2H-C structure (JCPDS file No. 41-1487) with only two preferred orientations on (0 0 2) and (0 0 4) planes. In addition, the peak at 27° is less broad compared with the (0 0 2) peak of graphene prepared by other methods due possibly to its relatively thick multilayer graphene structure and large

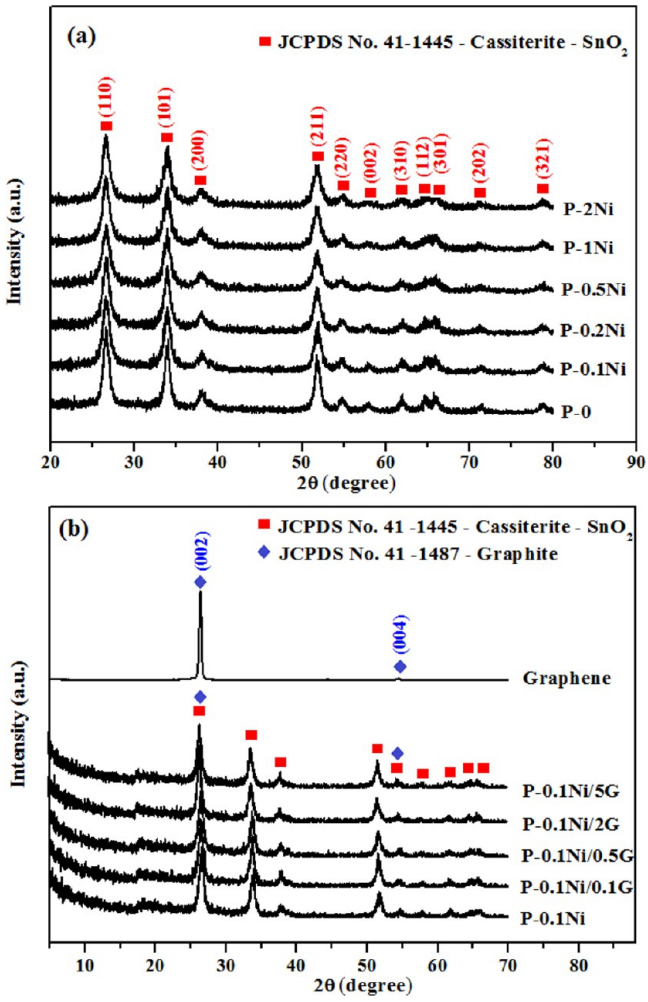

Figure 1. XRD patterns of (a) FSP-made Ni-doped SnO_2 nanopowders with different Ni doping levels (P-0 to P-2Ni) and (b) graphene-loaded 0.1 wt % Ni-doped SnO_2 nanopowders with different graphene loading levels (P-0.1Ni/0.1G to P-0.1Ni/5G).

crystallite size.[28−30] Moreover, the absence of graphene/graphite oxide peak at around 10° confirms that graphene is in the reduced state.[35,36] When 0.1 wt % Ni-doped SnO_2 nanopowders is loaded with 0.1−5 wt % graphene, the (0 0 2) and (0 0 4) graphitic peaks are overlapped with the (1 1 0) and (2 2 0) peaks of cassiterite SnO_2 such that the resulting diffraction patterns are not significantly different from the unloaded one. The result can be expected because the content of graphene is so low that the contributions of graphitic peaks are not clearly noticeable. It should be noted that structural characterizations of graphene-loaded materials have been primarily focused on 0.1 wt % Ni-doped SnO_2 nanoparticles (P-0.1Ni) because this Ni-doping level will provide optimal acetone-sensing performances.

Figure 2a,b shows GI-XRD patterns of sensing films made of SnO_2 doped with 0−2 wt % Ni (S-0 to S-2Ni) and 0.1 wt % Ni-doped SnO_2 nanoparticles loaded with 0−5 wt % graphene (S-0.1Ni and S-0.1Ni/0.1G to /5G) on the Au/Al_2O_3 substrate after annealing and sensing test, respectively. It is seen that the sensing films have similar crystallinity to their corresponding powders with peaks matched with the same JCPDS files and diffraction peaks of Ni are also absent. In addition, S-0 to S-2Ni and S-0.1Ni/0.1G to 5G films exhibit only a few dominant

DOI: 10.1021/acsami.5b00161
ACS Appl. Mater. Interfaces 2015, 7, 3077−3092

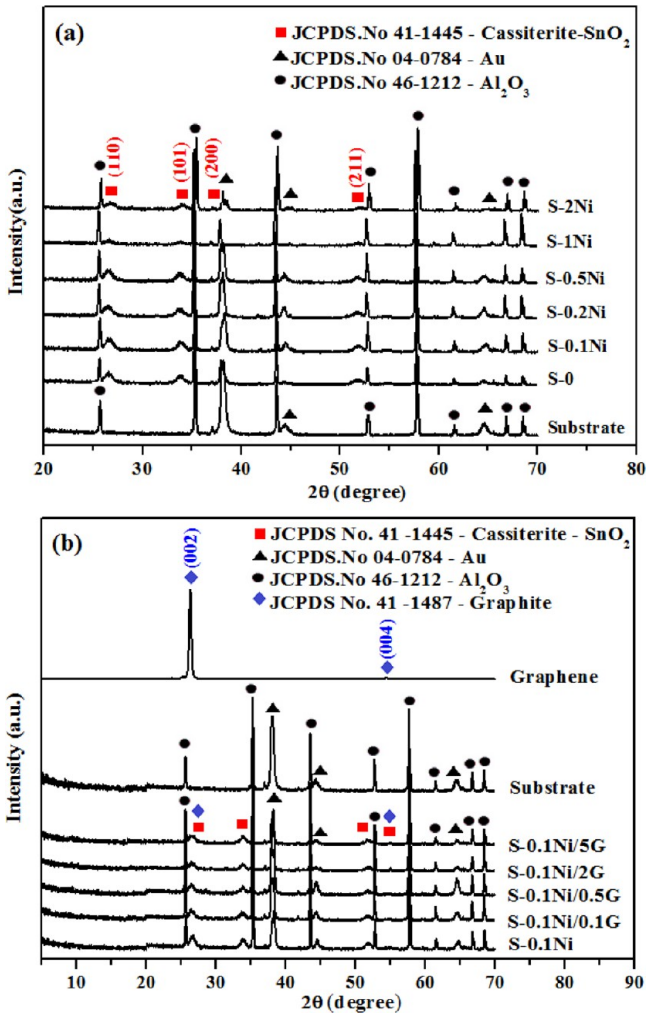

Figure 2. XRD patterns of sensing films based on (a) 0–2 wt % Ni-doped SnO_2 nanoparticles (S-0 to S-2Ni) and (b) 0.1 wt % Ni-doped SnO_2 loaded with 0.1–5 wt % graphene (S-0.1Ni/0.1G to S-0.1Ni/5G) on Au/Al_2O_3 substrates after annealing and sensing test.

planes of SnO_2 with similar relative XRD peak magnitudes compared with their corresponding nanopowders (P-0 to P-1Ni and P-0.1Ni/0.1G to 5G), indicating a relatively low amount of nanoparticles in the sensing films. The XRD peaks of the Al_2O_3 substrate (JCPDS file No. 46-1212) and Au electrode (JCPDS file No. 04-0784) are also present with relatively high magnitudes compared with those of sensing films due to a relatively low amount of sensor materials.

Figure 3 illustrates the bright-field (BF) and high-resolution (HR) TEM images of FSP-made undoped and 2 wt % Ni-doped SnO_2 nanoparticles (P-0 and P-2Ni). The corresponding selected area electron diffraction (SAED) patterns are shown in the inset. From the BF-TEM images (Figure 3a and 3c), undoped and Ni-doped SnO_2 nanoparticles are spherical and polyhedral with typical diameters ranging from 5 to 20 nm. In addition, they are nonagglomerated and well dispersed. The respective SAED patterns (inset) show polycrystalline diffraction rings corresponding to the (1 1 0), (1 0 1), (2 0 0), (2 1 1) and (3 0 1) lattice planes of the cassiterite SnO_2 structure, in accordance with those observed in the XRD patterns (Figure 1). The corresponding HR-TEM images (Figure 3b,d) clearly show lattice fringes on various nanoparticles whose *d*-spacings can be well matched with various planes of the tetragonal SnO_2 phase. Furthermore, it can be noticed that *d*-spacing of a given plane for P-2Ni tends to be slightly smaller than that for P-0, signifying a smaller lattice constant of the Ni-doped SnO_2 material due possibly of substitutional Ni-doping. The results are consistent with the Hume–Rothery rule and several studies of Ni-doped SnO_2 materials.[22−25] Based on this rule, Sn^{4+} with the ionic radius of 0.069 nm can be stably substituted with Ni^{3+} (high spin) and Ni^{2+} (low spin) (the ionic radii of 0.06 and 0.069 nm) because the differences of their effective ionic radii are much less than the limit of 15%. Thus, the decreased lattice spacing of the Ni-doped SnO_2 crystal may be attributed to substitution of the smaller nickel ions.

Typical BF-TEM and HR-TEM images of electrolytically exfoliated graphene are displayed in Figure 4a,b, respectively. The BF-TEM image shows a portion of smooth round-edge overlapped sheets with various shapes and sizes. The observed large background sheet is roughly polygonal with a few hundred nanometers in mean diameter and wavy edges whereas overlapped sheets contain rectangular stripes with 20–40 nm in width and more than 100 nm in length. The respective SAED pattern (inset) exhibits dotted diffraction rings that can be matched to (0 0 2), (1 0 2) and (1 0 3) planes of hexagonal graphite, indicating a randomly oriented graphitic crystal structure. The HR-TEM image further affirms that they are indeed multilayer graphene with 4–7 graphitic fringes observed on some edges. Figure 4c shows the BF-TEM image of 0.1 wt % Ni-doped SnO_2 nanoparticles loaded with 5 wt % graphene after annealing. The TEM sample was prepared by spin-coating of graphene–SnO_2 paste mixed in the organic binder as previously described in section 2.3 on a blank glass substrate. The resulting film was annealed at 450 °C to eliminate the organic binder and form the composite powder film. The powder film was then scraped off and dispersed in ethanol before dropping onto a carbon/copper TEM grid. It can be seen that the polyhedral SnO_2 nanoparticles are randomly dispersed around and cover a small area of the graphene sheets, which are partially overlapped among themselves. Thus, the Ni-doped SnO_2 nanoparticles tend to be isolated from larger graphene sheets after dispersion in ethanol. The corresponding SAED pattern displays dotted diffraction ring of hexagonal graphene structure mixed with relatively thick diffraction rings of polycrystalline Ni-doped SnO_2 nanoparticles, confirming coexistence of the two materials.

The BET specific surface area (SSA_{BET}) and effective BET-equivalent particle diameter (d_{BET}) of Ni-doped SnO_2 nanoparticles and graphene–0.1 wt % Ni-doped SnO_2 nanoparticles were determined as a function of Ni-doping and graphene-loading concentrations, as displayed in Figure 5a,b, respectively. It can be seen that SSA_{BET} increases considerably from 81.3 to 101.2 m^2/g with a small Ni-doping concentration of 0.1 wt %. As the Ni-doping concentration increases further from 0.1 to 2 wt %, the SSA_{BET} tends to decrease slowly (101.2 to 92.8 m^2/g) while d_{BET} varies inversely with SSA_{BET} (unloaded SnO_2, 10.6 nm; 0.1–2 wt %Ni/SnO_2, 8.5 to 9.4 nm). The results indicate that the Ni dopant considerably affects the nucleation of flame-made SnO_2 nanoparticles. The presence of the dopant may affect the primary particle size by influencing the initial cluster formation, sintering and growth rate in the initial flame stage. In addition, dopants at high concentrations may change the formation of the crystal structure in the later flame stage.[10] In the case of graphene–0.1 wt % Ni-doped SnO_2 nanoparticles (Figure 5b), it is evident that SSA_{BET} monotonically increases

DOI: 10.1021/acsami.5b00161
ACS Appl. Mater. Interfaces 2015, 7, 3077–3092

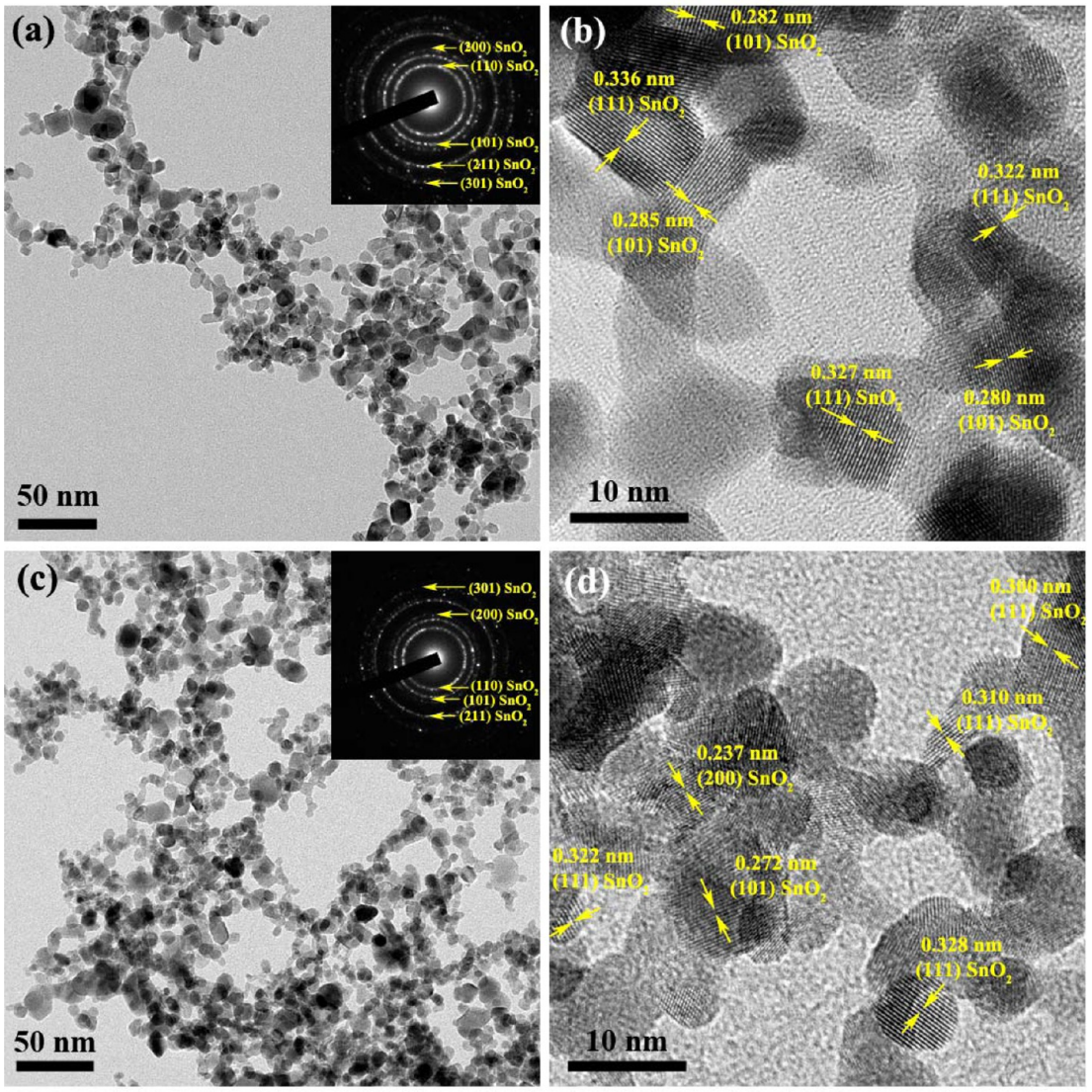

Figure 3. (a) BF-TEM and (b) HR-TEM images of FSP-made P-0. (c) BF-TEM and (d) HR-TEM images of P-2Ni. Insets: the corresponding SAED patterns.

from 101.2 to 110.9 m^2/g with increasing the graphene loading level from 0 to 5 wt % while d_{BET} correspondingly decreases from 8.5 to 8.1 nm, respectively. The increase of specific surface area may be attributed to the high surface area of graphene sheets that can act as spacer between nanoparticles, effectively preventing particle agglomeration and increasing the surface area. It should be noted that the value of d_{BET} for the graphene−0.1 wt % Ni-doped SnO_2 composite will be less accurate due to the presence of nonspherical particles like graphene.

Raman spectra of graphene (G) and 0.1 wt % Ni-doped SnO_2 nanoparticles loaded with graphene at various concentrations ranging from 0 to 5 wt % (P-0.1Ni, P-0.1Ni/0.1G to 5G) after binder-removal annealing are shown in Figure 6. With no graphene, 0.1 wt % Ni-doped SnO_2 nanoparticles exhibit a sharp Raman peak at ∼632 cm^{-1} corresponding to A_{1g} vibration mode of cassiterite SnO_2 crystal and two broad bands centered at ∼568 and ∼2,930 cm^{-1}, corresponding to mixed vibration modes of amorphous-phase tin oxide and high frequency vibration due to adsorbed water on SnO_2 (H_2O-SnO_2) surface, respectively.[37−39] In addition, the spectrum is almost the same as that of undoped SnO_2 one (omitted), indicating no additional vibration mode from Ni-doping. For the electrolytically exfoliated graphene powder, three carbon peaks are clearly seen at ∼1330, ∼1574 and ∼2648 cm^{-1}, which can be attributed to first-order vibration of the sp^3 bond (D mode), in-plane vibration of the sp^2 bond (G mode) and second-order vibration of the sp^3 bond (2D mode), respectively. In addition, the G peak is much higher and sharper than the 2D and D bands, respectively, implying highly ordered sp^2 lattice, low sp^3 edge defects and moderate second-order zone-boundary defects associated with good-quality multilayer graphene configuration.[40] With small graphene loading (0.1−0.5 wt %), the G peak become visible with low intensities while SnO_2 peaks remain about the same and the H_2O-SnO_2 peak begins to diminish. At high graphene loading level (2−5 wt %), G peak becomes dominant with higher intensity than A_{1g} SnO_2 peak while the 2D and D bands also rise accordingly with increasing graphene concentration and the H_2O-SnO_2 peak completely disappears. The results confirm that graphene retains its structural characteristics after mixing and annealing in air at 450 °C and does not oxidize into graphene oxide.

DOI: 10.1021/acsami.5b00161
ACS Appl. Mater. Interfaces 2015, 7, 3077−3092

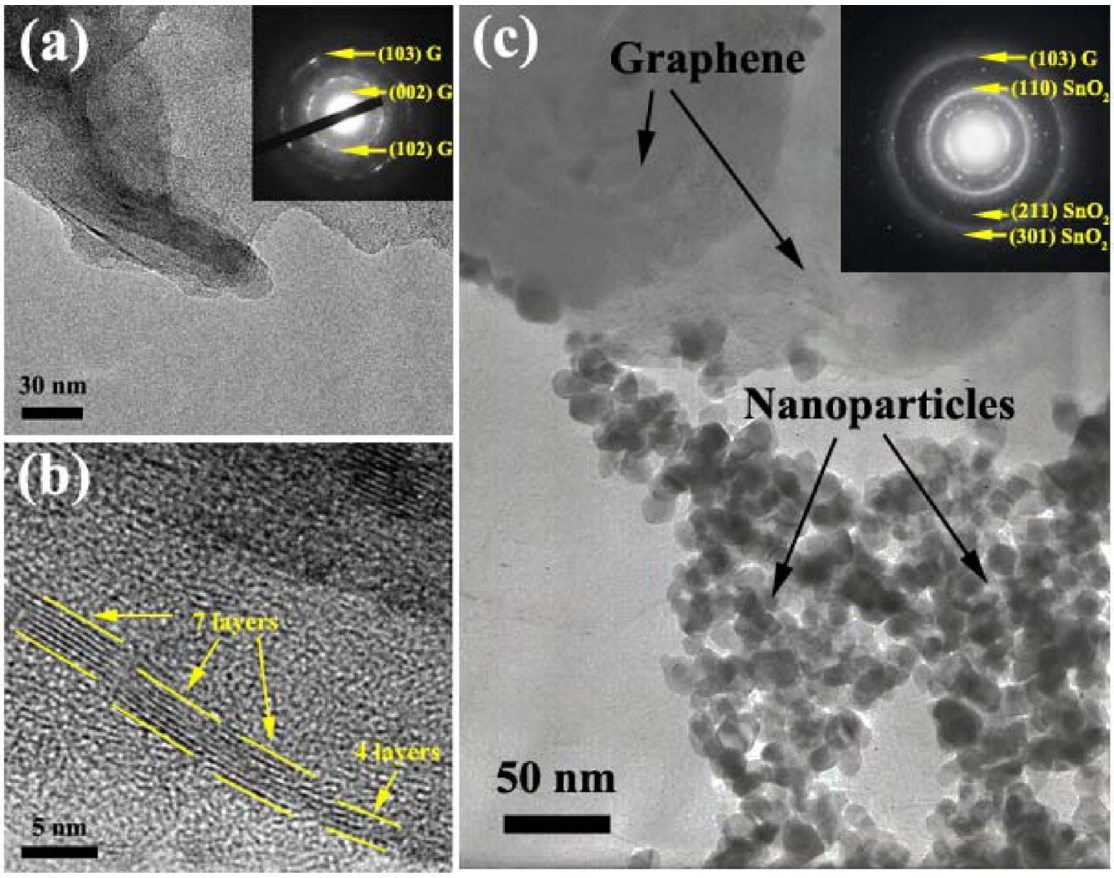

Figure 4. (a) BF-TEM and (b) HR-TEM images of electrolytically exfoliated graphene. (c) BF-TEM image of P-0.1Ni/5G. Insets: the corresponding SAED patterns.

The chemical compositions and oxidation states of existing elements in nanopowders and sensing films were determined by XPS. Figure 7 illustrates the representative high-resolution XPS spectra comprising Sn 3d, Ni 2p and O 1s core levels of 2 wt % Ni-doped SnO_2 nanopowder (P-2Ni, Figure 7a,c,e) and its sensing film (S-2Ni, Figure 7b,d,f) after annealing and sensing test. It should be noted that only XPS spectra of the 2 wt % Ni-doped SnO_2 nanopowder are presented because Ni 2p signals of SnO_2 nanopowders with lower Ni concentrations are less clear or absent due to the limited resolution of the XPS technique. The doublet components, Sn $3d_{5/2}$ and Sn $3d_{3/2}$, of the Sn 3d core level of P-2Ni (Figure 7a) are peaked at binding energies of 486.3 and 494.8 eV, respectively, while the corresponding values of S-2Ni (Figure 7b) are slightly shifted to 486.9 and 495.3 eV, respectively. The similar peaks of powder and sensing film can be both assigned to the highest oxidation state of Sn^{4+} for SnO_2.[23,41,42] The doublet components, Ni $2p_{3/2}$ and Ni $2p_{1/2}$, of the Ni 2p signal can be individually decomposed into two peaks, comprising a main peak and another minor peak at a higher binding energy, signifying the presence of two Ni species with different oxidation states. The Ni $2p_{3/2}$ and Ni $2p_{1/2}$ doublet peaks of P-2Ni (Figure 7c) contain main doublet peaks at 855.6 and 873.2 eV, and minor doublet peaks at 857.6 and 874.9 eV, respectively, while the corresponding two doublet peaks of S-2Ni (Figure 7d) are slightly moved to 856.3, 873.6, 857.8 and 874.9 eV, respectively. The main and minor doublet peaks can be assigned to Ni^{2+} (low spin) and Ni^{3+} (high spin) states, respectively.[41−46] Both Ni^{2+} and Ni^{3+} ions are expected to be at substitutional sites in SnO_2 lattice. The relative contributions of Ni^{2+} and Ni^{3+} oxidation states of P-2Ni are 78.6% and 21.4%, respectively while those of Ni^{2+} and Ni^{3+} for S-2Ni become 61.1% and 38.9%, respectively. This result reveals that some of Ni^{2+} ions are oxidized into Ni^{3+} ones after sensing test, suggesting partial oxidation of Ni in air. For oxygen element, the O 1s core level of P-2Ni (Figure 7e) can be deconvoluted into three contributions centered at 530.3 eV (main peak), 531.6 and 532.9 eV, while three O 1S contributions of S-2Ni (Figure 7f) are located at 530.9 (main peak), 532.1 and 532.9 eV, respectively. The main component of O 1s centered at 530.1−530.9 eV can be attributed to lattice oxygen (O^{2-}) of Ni-doped SnO_2 lattice on the outermost surface while the minor peak located at 531.6−532.1 eV may be assigned to the chemisorbed oxygen on SnO_2 surface and the minor peak centered at 532.9 eV may be ascribed to hydroxide surface groups due to water adsorption.[44−46]

The elemental compositions and oxidation states of graphene powder and 0.1 wt % Ni-doped SnO_2 sensing film loaded with 5 wt % graphene (S-2Ni/5G) were analyzed by XPS, as demonstrated in Figure 8. Figure 8a illustrates the XPS survey spectra of S-2Ni/5G and graphene powder. In the case of S-2Ni/5G, the spectrum confirms the expected Sn, Ni, C and O elements in the composite film as well as the Au element from electrodes. The Ni and C contents of S-2Ni/5G are determined to be 1.56 and 6.71 wt % (see the inset table), respectively, which are in fair agreement with the concentrations of input materials. For graphene prepared by electrolytic exfoliation, the spectrum demonstrates high-quality graphene with very low

DOI: 10.1021/acsami.5b00161
ACS Appl. Mater. Interfaces 2015, 7, 3077−3092

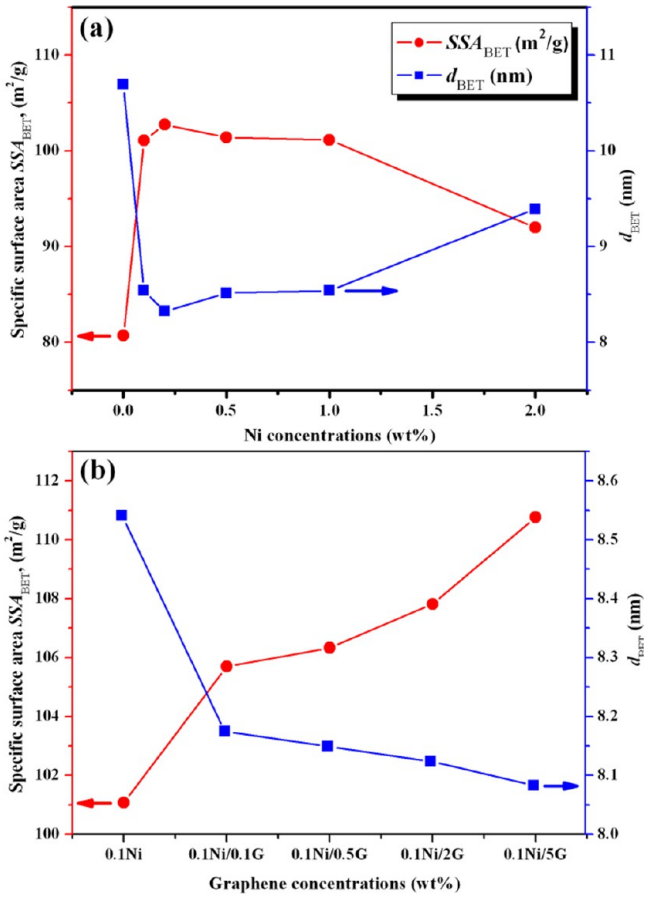

Figure 5. Specific surface area and average particle diameter of sensing films based on (a) 0−2 wt % Ni-doped SnO_2 nanoparticles (P-0 to P-2Ni) and (b) 0.1 wt % Ni-doped SnO_2 loaded with 0.1−5 wt % graphene (P-0.1Ni/0.1G to P-0.1Ni/5G) after annealing.

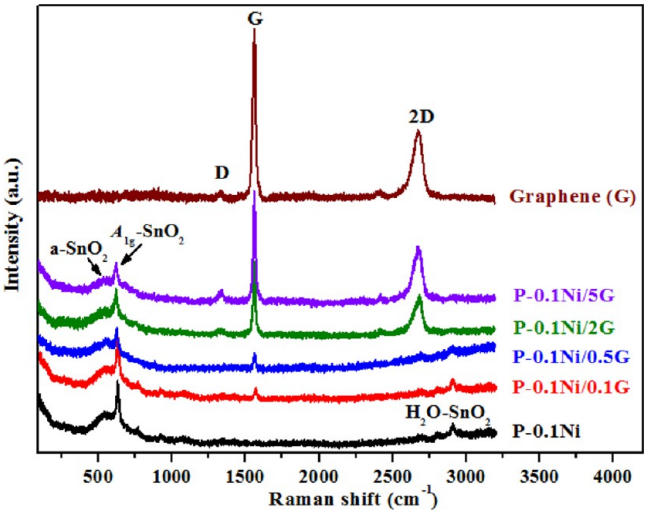

Figure 6. Raman spectra of electrolytically exfoliated graphene and graphene-loaded 0.1 wt % Ni-doped SnO_2 nanopowders with different graphene loading levels (P-0.1Ni and P-0.1Ni/0.1G to 5G).

oxygen content of ∼2 wt %, which is much lower than that of typical reduced graphene oxide prepared by various chemical synthesis methods.[47,48] The respective core level spectra for Sn 3d, Ni 2p, C 1s and O 1s of S-2Ni/5G are illustrated in Figure 8b−8e, respectively. The Sn 3d and Ni 2p spectra (Figure 8b,c) resemble closely those of S-2Ni (Figure 7b,d) with very similar binding energies and relative contributions of Ni^{2+} and Ni^{3+}, suggesting no chemical interaction between Ni-doped SnO_2 and graphene. For the C 1s carbon core level (Figure 8d), the asymmetric spectrum can be deconvoluted into one main peak at ∼284.9 eV associated with C—C bonding of main graphene lattice and two minor peaks at ∼286.6 and ∼288.5 eV corresponding to C—OH and C═O functional groups on the graphene surface, respectively.[47,48] The C 1s signal in the composite film bears a close resemblance with that of graphene powder (omitted), confirming that C 1s is mainly derived from graphene and not from surface contamination. Similarly, the O 1s spectrum (Figure 8e) consists of one main peak at 530.2 eV, which can be attributed to the lattice oxygen (O^{2-}) of Ni-doped SnO_2 nanoparticles,[46] and three minor peaks at 531.5, 532.4 and 533.3 eV, which may be ascribed to the C═O functional group from graphene, hydroxide functional group from SnO_2 nanoparticles and C—OH functional group from graphene, respectively.[46−48] The results also indicate that the presence of 5 wt % graphene considerably affects the contributions of oxygen species on the surface (see Figure 7f vs Figure 8e).

The cross-sectional SEM micrographs of S-0, S-0.1Ni, S-0.1Ni/0.1G, S-0.1Ni/0.5G, S-0.1Ni/2G and S-0.1Ni/5G sensing films on Al_2O_3 substrates equipped with Au interdigitated electrodes after annealing and sensing test are shown in Figure 9a−f, respectively. It can be seen that the undoped SnO_2 (S-0) and 0.1 wt % Ni-doped films (S-0.1Ni) similarly contain densely agglomerated nanoparticle layers with quite uniform thickness in the range of ∼14−16 μm. With graphene addition at low concentrations (S-0.1Ni/0.1G, S-0.1Ni/0.5G), the films are still dense but their thicknesses become less uniform and graphene sheets are still not clearly visible. At high graphene loading concentrations (S-0.1Ni/G2, S-0.1Ni/G5), the films become more porous with noticeable inclusion of graphene sheets and incidence of some voids within the films. The voids may occur due to distinct thermal expansion coefficients between large grains of graphene sheets and small grains of SnO_2 nanoparticles causing material separation after annealing heat treatment. Thicknesses of all sensing films are well controlled within the range of ∼12−18 μm, indicating good reproducibility of binder/powder mixing and spin-coating methods. Thus, FSP-made powder together with paste mixing and spin-coating technique has potential for the fabrication of graphene−metal oxide composite sensing films.

3.2. Acetone Sensing Properties. *3.2.1. Effect of Operating Temperature.* The effect of operating temperature ranging from 150 to 350 °C on the response to 200 ppm acetone (C_3H_6O) of SnO_2 nanoparticles with different Ni-doping and graphene loading concentrations are demonstrated in Figure 10a,b, respectively. With no graphene loading (Figure 10a), the responses of undoped and all Ni-doped SnO_2 sensors increase monotonically with increasing the operating temperature up to 350 °C. In particular, the 0.1 wt % Ni-doped SnO_2 sensor (S-0.1Ni) exhibits the highest response of ∼54.2 to 200 ppm acetone at the highest operating temperature of 350 °C. Thus, the 0.1 wt % Ni-doped SnO_2 sensor has been chosen based on its optimal response to acetone for further study with graphene loading, as illustrated in Figure 10b. It is seen that all graphene-loaded 0.1 wt % Ni-doped SnO_2 sensors also exhibit a monotonic increase of acetone response with increasing working temperature, and the response tends to increase with

DOI: 10.1021/acsami.5b00161
ACS Appl. Mater. Interfaces 2015, 7, 3077−3092

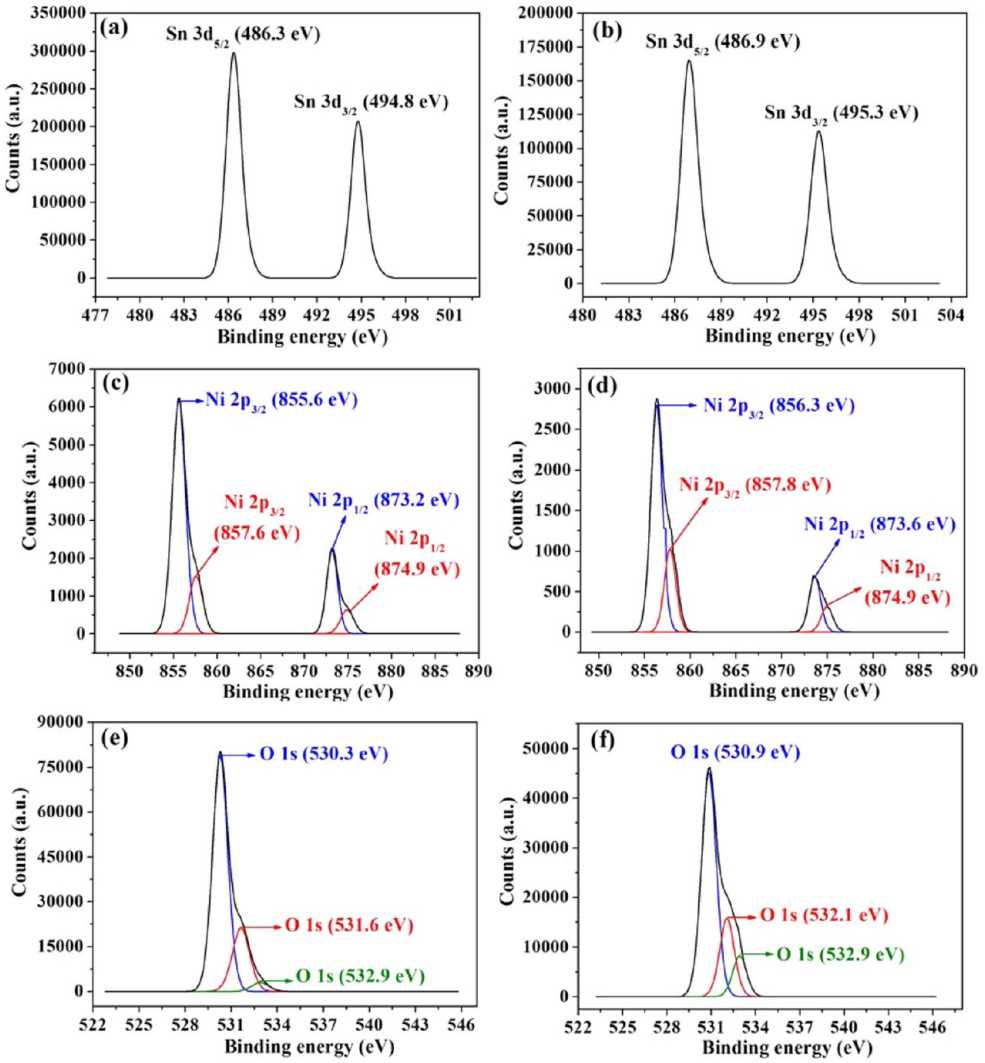

Figure 7. XPS spectra of (a) Sn 3d, (c) Ni 2p and (e) O 1s core levels for FSP-made 2 wt % Ni-doped SnO_2 nanopowder (P-2Ni). (b) Sn 3d, (d) Ni 2p and (f) O 1s core levels for sensing film after annealing and sensing test (S-2Ni).

increasing graphene loading levels, especially at high operating temperatures. In particular, the Ni-doped SnO_2 sensing film with 5 wt % graphene (S-0.1Ni/5G) sensor exhibits the highest response of ~169.7 to 200 ppm acetone at 350 °C, which is more than 3 times as high as that of unloaded one. The roles of operating temperature, Ni doping and graphene loading will be further discussed in subsequent sections.

3.2.2. Effect of Ni-Doping. Figure 11a shows the change in resistance of SnO_2 sensing films with different Ni doping concentrations (S-0 to S-2Ni) under exposure to various C_3H_6O concentrations at the highest operating temperature of 350 °C. It is seen that the baseline sensor resistance increases monotonically and drastically by almost 3 orders of magnitude as the Ni-doping level increases from 0 to 2 wt %. Similar doping dependence of baseline resistance is seen but the magnitude of resistance span is relatively less at a lower operating temperature. The increase of resistance with increasing Ni doping level may be explained based on substitutional-doping effect. Doping of Ni, a *p*-type dopant in SnO_2, generates holes, which will be neutralized by existing electrons of *n*-type SnO_2 host resulting in the decrease of electron concentration and increase of electrical resistance. At 2 wt % Ni-doping, the material is still *n*-type with a very low concentration of electrons. A higher Ni-doping level may lead to complete compensation and inversion to a *p*-type semiconductor, exhibiting a decrease in resistance with increasing Ni-doping concentration. However, Ni is more likely to precipitate into the secondary phase of *p*-type nickel oxide, which forms *p*−*n* heterojunctions that exhibit high electrical resistance.[12−23]

When exposed to C_3H_6O, the resistances of all sensors decrease rapidly, conforming to a typical *n*-type semiconducting characteristic toward a reducing gas. In addition, the resistance changes of the Ni-doped SnO_2 sensor with low Ni-doping levels (0.1−0.5 wt %) are considerably better than that of undoped one, whereas those of a sensor with high doping levels (1−2 wt %) are comparable or inferior compared with that of the undoped sensor. The corresponding sensor characteristics in terms of sensor response (solid line, left axis) and response time (dash line, right axis) of S-0 to S-2Ni sensors as a function of C_3H_6O concentration are displayed in Figure 11b. It is evident that the sensor response and response time initially improve with increasing Ni-doping concentration from 0 to 0.1 wt % but then steadily degrade as the concentration increases further to 2 wt %. In particular, the 0.1 wt % Ni-doped SnO_2 sensor (S-0.1Ni) exhibits the highest response of 54.2 to 200

DOI: 10.1021/acsami.5b00161
ACS Appl. Mater. Interfaces 2015, 7, 3077−3092

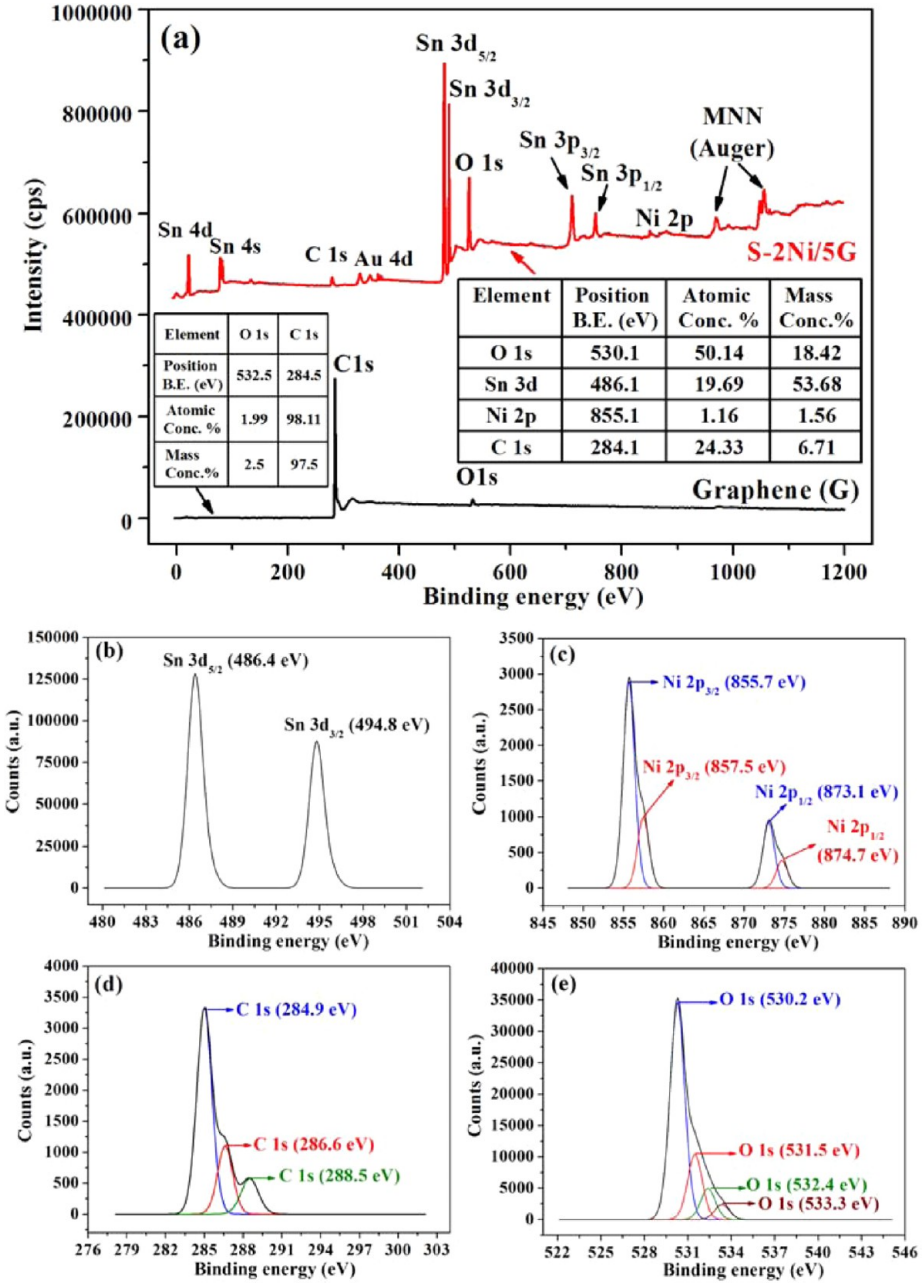

Figure 8. XPS spectra of graphene and S-2Ni/5G sensor sensing film after annealing and sensing test: (a) survey scan, (b) Sn 3d, (c) Ni 2p, (d) C 1s and (e) O 1s core levels.

ppm of C_3H_6O, which is more than 4 times as high as that of the undoped SnO_2 sensor (S-0) at 350 °C. Moreover, the response increases rapidly in the low range of C_3H_6O concentration (2.5−30 ppm) and then increases more slowly in the high range of C_3H_6O concentration (30−200 ppm), indicating the power-law behavior with the exponent value of <1. Furthermore, the 0.1 wt % Ni-doped SnO_2 sensor exhibits a short response time of ∼13 s while the recovery time (not shown) is also short, on the order of a few minutes. Therefore, 0.1 wt % is the optimum Ni-doping concentration that results in high and fast acetone-sensing response.

The role of Ni dopant on gas-sensing performances of SnO_2 nanoparticles may be explained based on its influence on specific surface area as well as its electronic and catalytic effects. From the BET results, it is seen that Ni doping at low concentration results in a considerable increase of the specific surface area by as much as 20%. Thus, the observed gas-sensing enhancement could be attributed to the increase of surface area. However, this mechanism alone should not be sufficient to explain the observed gas-sensing improvement by Ni because the increase of specific surface area is not as large as the increase of acetone response. Doping and related effects are then used to further explain the gas-sensing enhancement by Ni. In a typical *n*-type SnO_2 gas sensor, oxygen species (O_2^-, O^- and O^{2-}) are initially chemisorbed on the surface at elevated temperatures in air. With Ni dopants, Ni^{2+} and Ni^{3+} ions may substitute Sn sites in and on the SnO_2 surface via defect reactions of NiO and Ni_2O_3 quasi-molecules that can be represented in Kröger−Vink notation according to[35,36,49]

$$NiO \rightarrow Ni''_{Sn} + V_o^{\bullet\bullet} + O_o^x \quad (1)$$

DOI: 10.1021/acsami.5b00161
ACS Appl. Mater. Interfaces 2015, 7, 3077−3092

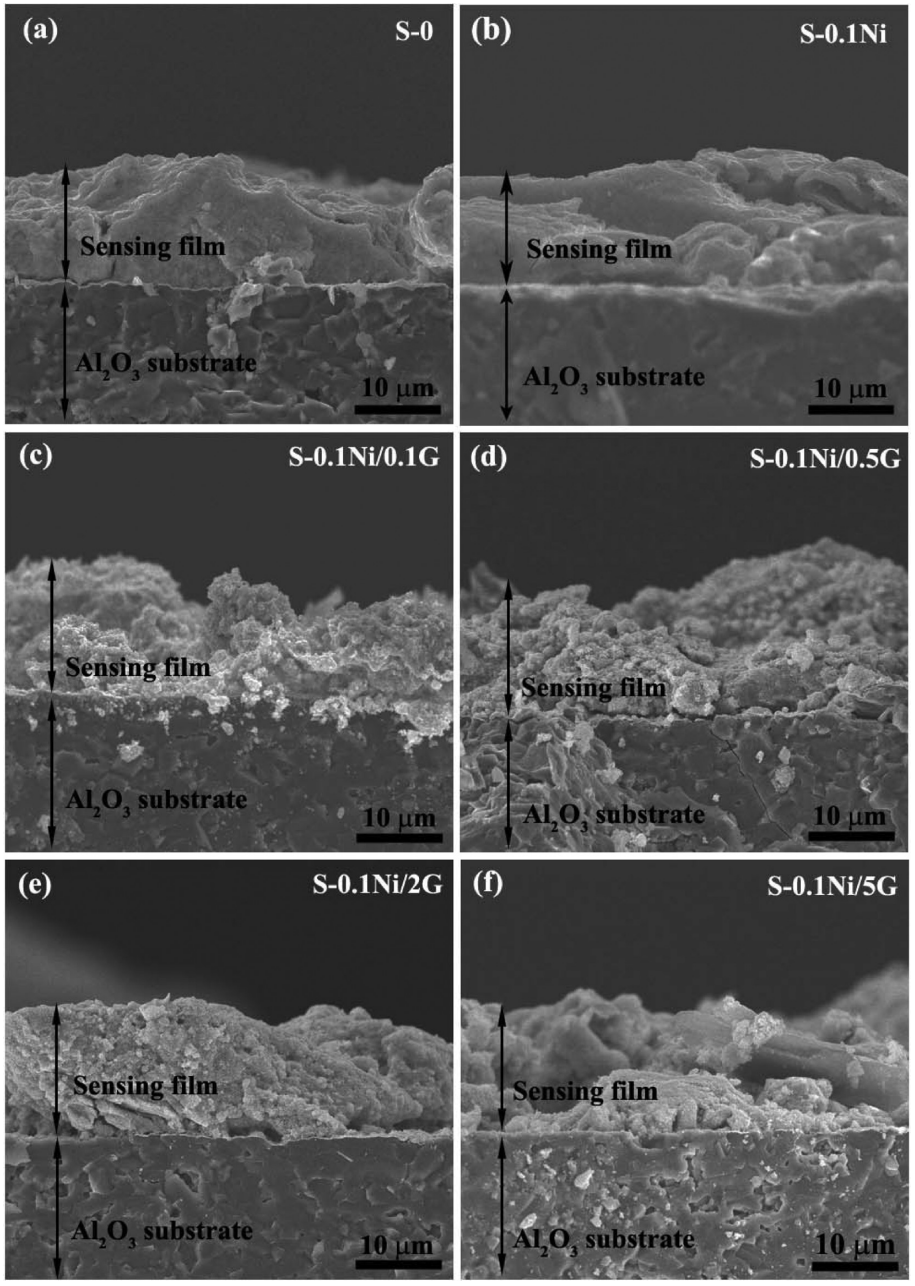

Figure 9. SEM images (cross-sectional view) of (a) S-0, (b) S-0.1Ni, (c) S-0.1Ni/0.1G, (d) S-0.1Ni/0.5G, (e) S-0.1Ni/2G and (f) S-0.1Ni/5G sensing films on Au/Al_2O_3 substrates after annealing and sensing test.

$$Ni_2O_3 \rightarrow 2Ni'_{Sn} + 2h^{\bullet} + 2O_o^{\,x} + \frac{1}{2}O_2 \quad (2)$$

where Ni''_{Sn}, Ni'_{Sn}, $V_o^{\bullet\bullet}$, $O_o^{\,x}$, O_2 and $h^{\bullet}$ are the Ni−Sn substitutional site with double negative charge, the Ni−Sn substitutional site with single negative charge, the oxygen vacancy with double positive charge, the neutral oxygen site, the oxygen gas molecule and the singly positive charge hole, respectively. The first process generates new oxygen vacancies and form $Ni^{2+}-V_o$ complexes while the latter induces positively charged holes that will be annihilated by existing electrons, leading to the increase of baseline resistance as observed in Figure 11a. From the results, the Ni^{3+} contribution in sensing film of around 39% can cause a considerable increase of resistance with Ni doping. Upon exposure to C_3H_6O, chemisorbed oxygen species particularly O^- and O^{2-} are directly reduced by gas molecules according to

$$8O^- + C_3H_6O \rightarrow 3H_2O + 3CO_2 + 8e^- \quad (3)$$

$$8O^{2-} + C_3H_6O \rightarrow 3H_2O + 3CO_2 + 16e^- \quad (4)$$

The reactions release electrons from these species into the conduction band of SnO_2, resulting in a resistance decrease. The reaction rates toward various reducing gases are primarily controlled by the availability and type of oxygen species as well as the reducing reaction rate of each gas molecule. O^{2-} is more reactive than O^- and generates double the amount of electrons per reaction, but it requires a relatively high activation energy. An undoped SnO_2 sensor typically has an optimal operating temperature at 300−350 °C when the adsorption/desorption rate ratio of O^- and O^{2-} is maximized. From the observed

DOI: 10.1021/acsami.5b00161
ACS Appl. Mater. Interfaces 2015, 7, 3077−3092

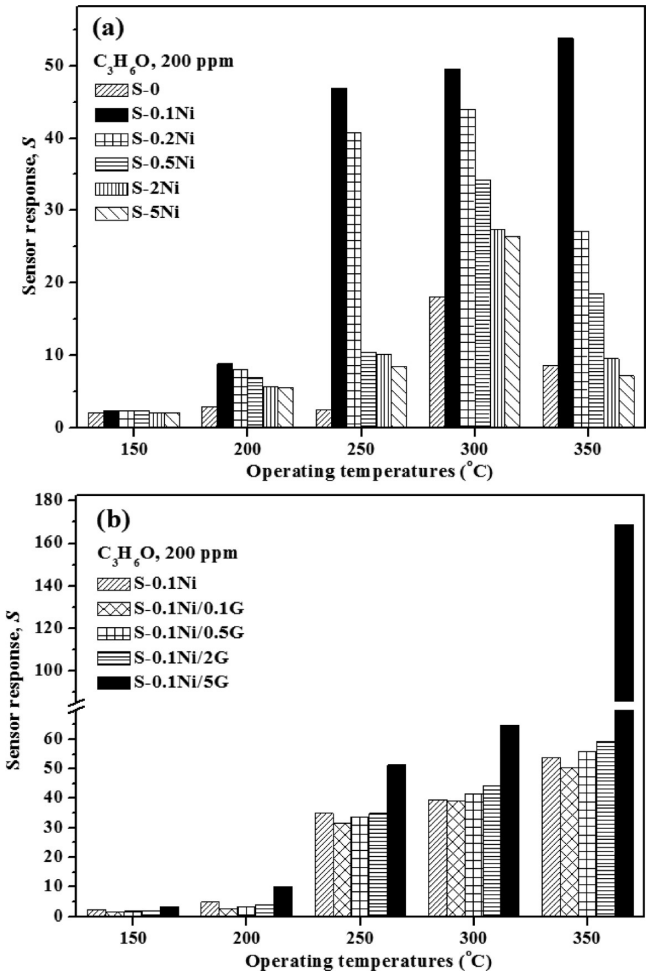

Figure 10. Histograms of sensor response to 200 ppm of C_3H_6O of (a) FSP-made Ni-doped SnO_2 sensor (S-0 to S-2Ni) with different Ni-doping levels and (b) graphene-loaded 0.1 wt % Ni-doped SnO_2 nanopowders with different graphene loading levels (S-0.1Ni and S-0.1Ni/0.1G to 5G) at various operating temperatures ranging from 150 to 350 °C.

results, the optimal operating temperature of Ni-doped sensors is still in the same range as that of the undoped one, implying similar temperature dependency of adsorption/desorption of oxygen species on the Ni-doped SnO_2 surface. The enhancement of acetone responses with Ni doping at low concentrations (0.1−0.2 wt %) may be attributed to the increased density of O^- and especially O^{2-} adsorption sites on nanoparticle surfaces due to additional oxygen vacancies formed in $Ni^{2+}-V_o$ complexes, which directly enhance the formation of oxygen species at high temperature.[35] In addition, the reduced background electron concentration due to Ni (*p*-type) doping also facilitates electron transfer from gas molecules to conduction band, allowing much larger change in resistance. At higher Ni doping levels (0.5−2 wt %), the acetone response reduces substantially compared with the optimally doped one. The unfavorable characteristic may be caused by the high-level surface disorder on nanoparticle surfaces induced by the heavy Ni doping. This assumption is well supported by the XPS data that 61% of Ni dopants become Ni^{2+} ions and generate more vacancy defects at the highest Ni-doping level of 2 wt %. The surface disorder can be represented as defective surface states that trap charge carries, causing pinning of Fermi-level, less change of surface conductivity due to charge transfer from reducing reaction and deteriorated gas response.[35,49]

3.2.3. Effect of Graphene Loading. The influence of graphene loading level on the sensing performances toward C_3H_6O of Ni-doped SnO_2 nanoparticles with the optimal Ni-doping content of 0.1 wt % is further investigated, as shown in Figure 11c,d. Figure 11c demonstrates the change in resistance of 0.1 wt % Ni-doped SnO_2 sensing films with different graphene loading concentrations ranging from 0 to 5 wt % under exposure to various C_3H_6O concentrations at 350 °C. It can be seen that the baseline sensor resistance increases substantially by more than 1 order of magnitude with increasing the graphene loading level from 0 to 0.5 wt % (S-0.1Ni, S-0.1Ni/0.1G to 0.5G). In contrast, the baseline resistance decreases gradually as the graphene loading concentration increases further from 0.5 to 5 wt %. This trend of baseline resistance is similarly observed at other operating temperatures. The initial increase of resistance with increasing graphene loading level may be explained based on the effect of metal−semiconductor (M−S: graphene−Ni-doped SnO_2 nanoparticles) junctions. At low graphene concentrations (0.1−0.5 wt %), conductive graphene sheets are separately dispersed within the SnO_2 matrix and form M/S junctions, leading to enhanced depletion regions in SnO_2 nanoparticles and increased resistivity with increasing graphene concentration. When the graphene loading level becomes relatively high, graphene sheets begin to form clusters, which are partially connected as observed from SEM images (Figure 9e,f). Thus, partially connected conductive network of graphene may be formed, leading to the decrease in electrical resistance.

Upon C_3H_6O exposure, all sensors display a typical decrease of resistance in response to a reducing gas of *n*-type semiconductor gas sensors. In addition, the resistance change of the sensor is initially slightly decreased and then progressively increased with increasing the graphene loading concentration from 0.1 to 5 wt %. Moreover, the 5 wt % graphene-loaded sensor demonstrates relatively fast changes in resistance, response stabilization and baseline recovery compared with other sensors. It should be noted that the composite with higher graphene loading level (i.e., 10 wt %) have also been tested and found to have very poor sensor response due to excessive aggregation/agglomeration of graphene leading to too high material conductivity and insignificant resistance change upon gas exposure. Therefore, it can be primarily concluded that the optimal graphene loading level for graphene−Ni-doped SnO_2 sensor is 5 wt %.

Figure 11d shows the corresponding sensing characteristics in terms of sensor response (solid line, left axis) and response time (dash line, right axis) of S-0.1Ni and S-0.1Ni/0.1G to 5G as a function of C_3H_6O concentration. It can be seen that the sensor response and response time are initially slightly degraded and then monotonically improved with increasing graphene loading concentration from 0.1 to 5 wt %. In particular, the S-0.1Ni/5G sensor exhibits high acetone-sensing performances at 350 °C in terms of response (S = 169.7 at 200 ppm) and response time (t_{res} = 5.3 s) compared with S-0.1Ni/2G (S = 61.3, t_{res} = 24 s), S-0.1Ni/0.5G (S = 56.6, t_{res} = 42 s), S-0.1Ni/0.1G (S = 52.4, t_{res} = 35 s) and S-0.1Ni (S = 54.2, t_{res} = 13 s). In addition, graphene incorporation also results in the reduction of recovery time for the Ni-doped SnO_2 sensor. Additionally, the response characteristics as a function of acetone concentration of graphene-loaded Ni-doped SnO_2 sensors conform to the well-known power law with exponent

DOI: 10.1021/acsami.5b00161
ACS Appl. Mater. Interfaces 2015, 7, 3077−3092

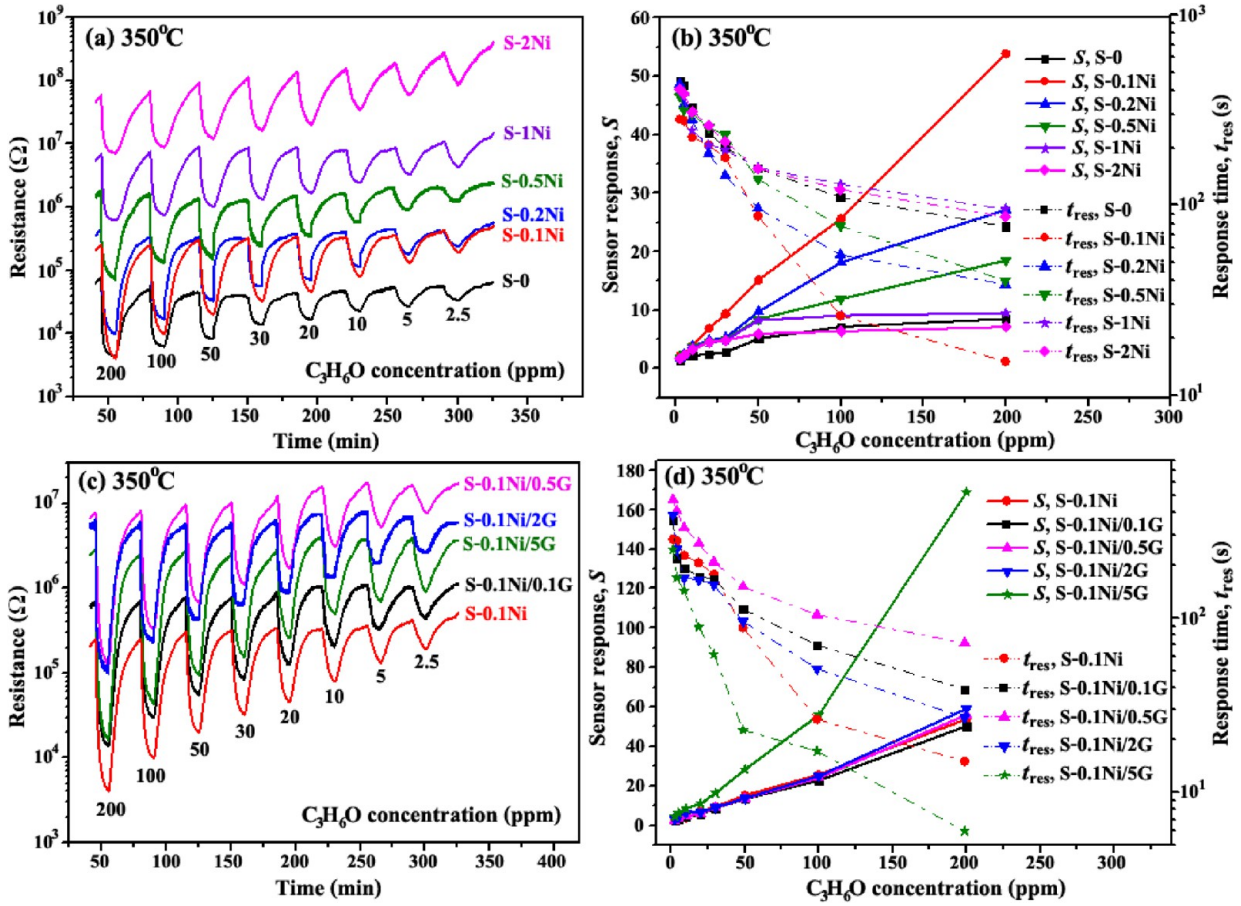

Figure 11. (a) Change in resistance, (b) correlation of sensor response (solid line, left axis) and response time (dash line, right axis) vs acetone concentration of S-0 to S-2Ni sensors at 350 °C. (c) Change in resistance and (d) correlation of sensor response (solid line, left axis) and response time (dash line, right axis) vs acetone concentration of S-0.1Ni and S-0.1Ni/0.1G to 5G sensors at 350 °C.

value >1. Furthermore, the S-0.1Ni/5G sensor still exhibits a high response of ∼6.3 at a low acetone concentration of 5 ppm corresponding to a very low acetone detection limit of ∼0.04 ppm (predicted at the response of 1.1 based on the power-law fitting). Thus, the optimal sensor is sensitive at low acetone concentrations and promising for the acetone analysis in breath. Moreover, the 5 wt % graphene-loaded 0.1 wt % Ni-doped SnO_2 sensor exhibits relatively high acetone response compared with several other VOC sensors listed in Table 1, which reported the response in the range of 3−50 to 200 ppm acetone. Therefore, the graphene−Ni-doped SnO_2 composite is a highly promising material for acetone sensing applications.

The substantial gas-sensing enhancement by graphene may be explained based on the following plausible mechanisms. First, graphene could provide extra surface area for adsorption sites and reaction with target gases since the surface of graphene is reported to be active to various reducing and oxidizing gases, leading to enhanced sensor response.[28−31] From BET results (Figure 5), it is evident that the specific surface area of the composite increases considerably with increasing graphene-loading concentration. Second, graphene could prevent agglomeration of SnO_2 nanoparticles via the intercalation effect as previously observed in SEM images (Figure 9e,f), resulting in large effective surface area and considerably improved gas-sensing performances.

Furthermore, graphene should form M−S junctions with Ni-doped SnO_2 nanoparticles that could enhance electronic interaction with the target gas. The Ni-doped SnO_2−graphene junctions would induce depletion regions due to their work function difference in addition to the first depletion region created on the surface of Ni-doped SnO_2 nanoparticles by chemisorbed oxygen species (O^- and O^{2-}). The interaction between gas molecules and the surface of Ni-doped SnO_2 nanoparticles will modify the first depletion layer while other gas molecules can also adsorb on graphene and transfer electrons to alter the depletion layers at the Ni-doped SnO_2−graphene interfaces.[36] Thus, the electronic interaction between SnO_2 and graphene effectively facilitates the gas detection through the change in the electrical conductivity of the nanohybrid. The surface accessibility between FSP-made nanoparticles and graphene will play the key role to the enhanced response because the operation involves adsorption/desorption processes at the interface. Moreover, the formation of graphene−Ni-doped SnO_2 nanoparticle interfaces could lead to additional active gas-adsorption sites (such as vacancies, point defects, oxygen functional groups as well as the sp^2-bonded carbon) due to chemical interaction between surface atoms of two materials and thereby greatly improves the sensor response.[30]

Additionally, graphene's high electrical conductivity can result in the fast transport of electrons from gas interaction in the sensing layer, leading to the decrease of response and recovery times. The graphene loaded in Ni-doped SnO_2 sensing films should enhance the local material conductivity and electron transport since graphene is zero-band gap metal with very high electron mobility.[28−31] This is in accordance with the

DOI: 10.1021/acsami.5b00161
ACS Appl. Mater. Interfaces 2015, 7, 3077−3092

results in Figure 11c that the baseline resistance (inverse of conductivity) of graphene-loaded Ni-doped SnO_2 sensing film tends to decrease at the high graphene loading levels of 1−2 wt %. The increase in conductivity by graphene could assist electron transfer from the gas reaction, leading to enhanced response and response rate at a given temperature, as previously seen in Figures 10 and 11. However, it does not result in a reduction of optimal operating temperature because the additional active gas-adsorption sites provided by the graphene−Ni-doped SnO_2 nanoparticle interfaces should be thermally activated so that the gas adsorption reaction is further enhanced with increasing operating temperature.

3.2.4. Selectivity, Repeatability and Reproducibility. The selectivity of undoped, Ni-doped SnO_2 and graphene-loaded Ni-doped SnO_2 sensing films has been evaluated for C_3H_6O, C_2H_5OH, H_2, CH_4, H_2S and NO_2 at a low gas concentration of 5 ppm and the operating temperature of 350 °C, as illustrated in Figure 12. It can be seen that Ni-doping and graphene

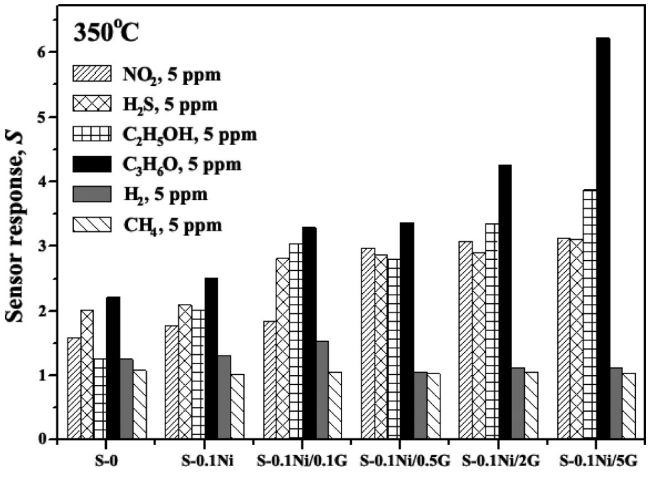

Figure 12. Selectivity histograms of sensor responses to 5 ppm of NO_2, H_2S, C_2H_5OH, C_3H_6O, H_2 and CH_4 of S-0, S-0.1Ni, S-0.1Ni/0.1G, S-0.1Ni/0.5G, S-0.1Ni/2G and S-0.1Ni/5G sensors at 350 °C.

loading considerably affect the acetone selectivity of FSP-made SnO_2 nanoparticles. In the absence of Ni-doping and graphene loading, SnO_2 nanoparticles exhibit medium responses to C_3H_6O, NO_2 and H_2S and low responses to CH_4, C_2H_5OH and H_2. With the optimal Ni-doping concentration of 0.1 wt %, responses to C_3H_6O, C_2H_5OH and NO_2 increase considerably but the response enhancement for acetone is more substantial than others while the responses to CH_4, H_2 and H_2S are only slightly increased. Thus, the acetone selectivity of the FSP-made SnO_2 sensor is considerably improved with the optimal Ni doping.

With very small graphene loading of 0.1−0.5 wt %, the responses to C_3H_6O, C_2H_5OH and H_2S increase moderately whereas those to other gases are or not much affected, and thus the acetone selectivity is slightly improved. As the graphene loading level increases from 0.5 to 5 wt %, response to C_3H_6O increases rapidly whereas that to C_2H_5OH also increases but with a much smaller rate, and those to other gases are not significantly changed, indicating the significant enhancement of the acetone selectivity with increasing graphene loading level. At the optimal graphene loading level of 5 wt %, the acetone response becomes about 2 times as high as that to ethanol. Thus, 5 wt % graphene-loaded Ni-doped SnO_2 exhibits not only high response but also high acetone selectivity against ethanol and other gases at a low gas concentration of 5 ppm. The observed high acetone selectivity suggests specifically high interaction rate between acetone vapor and graphene−Ni-doped SnO_2 nanoparticles interfaces. Lastly, the repeatability and reproducibility of the sensors, particularly S-0.1Ni and S-0.1Ni/5G, were evaluated. Each sensor showed good repeatability with less than 18% response variation from ten repeated measurements at the same gas concentration. In addition, five sensors from the same batch were found to have fair response variation of less than 27% tested under the same conditions.

4. CONCLUSIONS

In conclusion, FSP-made SnO_2 nanoparticles doped with Ni (0−2 wt %) and loaded with electrolytically exfoliated graphene (0.1−5 wt %) have been systemically studied for acetone-sensing applications. Characterizations by XRD, SEM, TEM, HRTEM, Raman spectroscopy and XPS revealed that Ni-doped SnO_2 nanostructures had a spheriodal morphology with a polycrystalline tetragonal SnO_2 phase, and nickel should form the solid solution with the SnO_2 lattice while graphene in the sensing film after annealing and testing still retained a high-quality nonoxidized sp^2 structure. The acetone response of the SnO_2 sensing film was found to be substantially improved up to 54.2 at 200 ppm and 350 °C with the lowest Ni-doping level of 0.1 wt % but further increase of Ni-doping concentration resulted in deteriorated acetone response. In contrast, the acetone response tended to be substantially enhanced with increasing the graphene loading level up to 5 wt %. The 5 wt % graphene-loaded 0.1 wt % Ni-doped SnO_2 sensor exhibited notably high acetone response of 169.7 to 200 ppm acetone with a short response time of ~5.4 s at the optimal operating temperature of 350 °C. The enhanced acetone-sensing performances of Ni-doped SnO_2 nanoparticles loaded with graphene may be attributed to large specific surface area of the composite structure, specifically high interaction rate between acetone vapor and graphene−Ni-doped SnO_2 nanoparticles interfaces and high electronic conductivity of graphene. Therefore, the graphene loaded Ni-doped SnO_2 sensor is a promising candidate for fast, sensitive and selective detection of acetone.

AUTHOR INFORMATION

Corresponding Author

*C. Liewhiran. E-mail: chaikarn_l@yahoo.com. Tel.: +66-81-408-2324. Fax: +66-53-892-271.

Notes

The authors declare no competing financial interest.

ACKNOWLEDGMENTS

The authors gratefully acknowledge the financial support from Thailand Graduate Institute of Science and Technology (TGIST-01-56-023), the Thailand Research Fund (TRF), the National Research University Project under the Office of the Higher Education Commission (CHE), Ministry of Education, the Graduate School, the Materials Science Research Center and Department of Physics and Materials Science, Faculty of Science, Chiang Mai University. Special thanks is given to the National Nanotechnology Center, NSTDA, Ministry of Science and Technology, through its program of Center of Excellence Network, Thailand for electron microscopy facilities and

DOI: 10.1021/acsami.5b00161
ACS Appl. Mater. Interfaces 2015, 7, 3077−3092

National Electronics and Computer Technology Center (NECTEC), Pathumthani, Thailand for the sensor facility.

REFERENCES

(1) Inyawilert, K.; Wisitsora-at, A.; Tuantranont, A.; Singjai, P.; Phanichphant, S.; Liewhiran, C. Ultra-Rapid VOCs Sensors Based on Sparked-In_2O_3 Sensing Films. *Sens. Actuators, B* **2014**, *192*, 745−754.

(2) Boeglin, M. L.; Wessels, D.; Henshel, D. An Investigation of the Relationship between Air Emissions of Volatile Organic Compounds and the Incidence of Cancer in Indiana Counties. *Environ. Res.* **2006**, *100*, 242−254.

(3) Arakawa, T.; Wang, X.; Kajiro, T.; Miyajima, K.; Takeuchi, S.; Kudo, H.; Yano, K.; Mitsubayashi, K. A Direct Gaseous Ethanol Imaging System for Analysis of Alcohol Metabolism from Exhaled Breath. *Sens. Actuators, B* **2013**, *186*, 27−33.

(4) Park, J. K.; Yee, H. J.; Lee, K. S.; Lee, W. Y.; Shin, Mh.; Kim, T. H.; Kim, S. R. Determination of Breath Alcohol Using a Differential-Type Amperometric Biosensor Based on Alcohol Dehydrogenase. *Anal. Chim. Acta* **1999**, *390*, 83−91.

(5) Song, P.; Wang, Q.; Yang, Z. Preparation, Characterization and Acetone Sensing Properties of Ce-Doped SnO_2 Hollow Spheres. *Sens. Actuators, B* **2012**, *173*, 839−846.

(6) Nasution, T. I.; Nainggolan, I.; Hutagalung, S. D.; Ahmad, K. R.; Ahmad, Z. A. The Sensing Mechanism and Detection of Low Concentration Acetone Using Chitosan-based Sensors. *Sens. Actuators, B* **2013**, *177*, 522−528.

(7) Chang, Y.; Yao, Y.; Wang, B.; Luo, H.; Li, T.; Zhi, L. Reduced Graphene Oxide Mediated SnO_2 Nanocrystals for Enhanced Gas-Sensing Properties. *J. Mater. Sci. Technol.* **2013**, *29*, 157−160.

(8) Liewhiran, C.; Tamaekong, N.; Wisitsoraat, A.; Phanichphant, S. Highly Selective Environmental Sensors Based on Flame-Spray-Made SnO_2 Nanoparticles. *Sens. Actuators, B* **2012**, *163*, 51−60 . 33.

(9) Sahm, T.; Mädler, L.; Gurlo, A.; Barsan, N.; Pratsinis, S. E.; Weimar, U. Flame Spray Synthesis of Tin Dioxide Nanoparticles for Gas Sensing. *Sens. Actuators, B* **2004**, *98*, 148−153.

(10) Height, M. J.; Mädler, L.; Pratsinis, S. E. Nanorods of ZnO Made by Flame Spray Pyrolysis. *Chem. Mater.* **2006**, *18*, 572−578.

(11) Tamaekong, N.; Liewhiran, C.; Wisitsora-at, A.; Phanichphant, S. Acetylene Sensor Based on Pt/ZnO Thick Films as Prepared by Flame Spray Pyrolysis. *Sens. Actuators, B* **2011**, *152*, 155−161.

(12) Mueller, R.; Mädler, L.; Pratsinis, S. E. Nanoparticle Synthesis at High Production Rates by Flame Spray Pyrolysis. *Chem. Eng. Sci.* **2003**, *58*, 1969−1976.

(13) Pawar, R. C.; Shaikh, J. S.; Moholkar, A. V.; Pawar, S. M.; Kim, J. H.; Patil, J. Y.; Suryavanshi, S. S.; Patil, P. S. Surfactant Assisted Low Temperature Synthesis of Nanocrystalline ZnO and Its Gas Sensing Properties. *Sens. Actuators, B* **2010**, *151*, 212−218.

(14) Pawar, R. C.; Lee, J.-W.; Patil, V. B.; Lee, C. S. Synthesis of Multi-Dimensional ZnO Nanostructures in Aqueous Medium for the Application of Gas Sensor. *Sens. Actuators, B* **2013**, *187*, 323−330.

(15) Pawar, R. C.; Shaikh, J. S.; Suryavanshi, S. S.; Patil, P. S. Growth of ZnO Nanodisk, Nanospindles and Nanoflowers for Gas Sensor: pH Dependency. *Curr. Appl. Phys.* **2012**, *12*, 778−783.

(16) Mädler, L.; Roessler, A.; Pratsinis, S. E.; Sahm, T.; Gurlo, A.; Barsan, N.; Weimar, U. Direct Formation of Highly Porous Gas-Sensing Films by in Situ Thermophoretic Deposition of Flame-Made Pt/SnO_2 Nanoparticles. *Sens. Actuators, B* **2006**, *114*, 283−295.

(17) Liewhiran, C.; Tamaekong, N.; Wisitsoraat, A.; Tuantranont, A.; Phanichphant, S. Ultra-Sensitive H_2 Sensors Based on Flame-Spray-Made Pd-Loaded SnO_2 Sensing Films. *Sens. Actuators, B* **2013**, *176*, 893−905 . 31.

(18) Patil, S. B.; Patil, P. P.; More, M. A. Acetone Vapour Sensing Characteristics of Cobalt-Doped SnO_2 Thin Films. *Sens. Actuators, B* **2007**, *125*, 126−130.

(19) Galatsis, K.; Cukrov, L.; Wlodarski, W.; McCormick, P.; Kalantar-zadeh, K.; Comini, E.; Sberveglieri, G. *p*- and *n*-Type Fe-Doped SnO_2 Gas Sensors Fabricated by the Mechanochemical Processing Technique. *Sens. Actuators, B* **2003**, *93*, 562−565.

(20) Jain, K.; Pant, R. P.; Lakshmikumar, S. T. Effect of Ni Doping on Thick Film SnO_2 Gas Sensor. *Sens. Actuators, B* **2006**, *113*, 823−829.

(21) Bagal, L. K.; Patil, J. Y.; Mulla, I. S.; Suryavanshi, S. S. Studies on the Resistive Response of Nickel and Cerium-Doped SnO_2 Thick Films to Acetone Vapor. *Ceram. Int.* **2012**, *38*, 6171−6179.

(22) Chen, Y.; Yu, L.; Feng, D.; Zhuo, M.; Zhang, M.; Zhang, E.; Xu, Z.; Li, Q.; Wang, T. Superior Ethanol-Sensing Properties Based on Ni-Doped SnO_2 *p*−*n* Heterojunction Hollow Spheres. *Sens. Actuators, B* **2012**, *166*−*167*, 61−67.

(23) Liu, X.; Zhang, J.; Guo, X.; Wu, S.; Wang, S. Enhanced Sensor Response of Ni-Doped SnO_2 Hollow Spheres. *Sens. Actuators, B* **2011**, *152*, 162−167.

(24) Lee, S. C.; Choi, H. Y.; Lee, S. J.; Lee, W. S.; Huh, J. S.; Lee, D. D.; Kim, J. C. Novel SnO_2-based Gas Sensors Promoted with Metal Oxides for the Detection of Dichloromethane. *Sens. Actuators, B* **2009**, *16*, 446−452.

(25) Cheng, J. P.; Wang, B. B.; Zhao, M. G.; Liu, F.; Zhang, X. B. Nickel-Doped Tin Oxide Hollow Nanofibers Prepared by Electrospinning for Acetone Sensing. *Sens. Actuators, B* **2014**, *190*, 78−85.

(26) Basu, S.; Bhattacharyya, P. Recent Developments on Graphene and Graphene Oxide based Solid State Gas Sensors. *Sens. Actuators, B* **2012**, *173*, 1−21.

(27) Ratinac, K. R.; Yang, W.; Ringer, S. P.; Braet, F. Toward Ubiquitous Environmental Gas Sensors-Capitalizing on the Promise of Graphene. *Environ. Sci. Technol.* **2010**, *44*, 1167−1176.

(28) Meng, F. L.; Li, H. H.; Kong, L. T.; Liu, J. Y.; Jin, Z.; Li, W.; Jia, Y.; Liu, J. H.; Huang, X. J. Parts Per Billion-Level Detection of Benzene Using SnO_2/Graphene Nanocomposite Composed of Sub-6nm SnO_2 Nanoparticles. *Anal. Chim. Acta* **2012**, *736*, 100−107.

(29) Lin, Q.; Li, Y.; Yang, M. Tin Oxide/Graphene Composite Fabricated via a Hydrothermal Method for Gas Sensors Working at Room Temperature. *Sens. Actuators, B* **2012**, *173*, 139−147.

(30) Zhang, H.; Feng, J.; Fei, T.; Liu, S.; Zhang, T. SnO_2 Nanoparticles-Reduced Graphene Oxide Nanocomposites for NO_2 Sensing at Low Operating Temperature. *Sens. Actuators, B* **2014**, *190*, 472−478.

(31) Chang, Y.; Yao, Y.; Wang, B.; Luo, H.; Li, T.; Zhi, L. Reduced Graphene Oxide Mediated SnO_2 Nanocrystals for Enhanced Gas-Sensing Properties. *J. Mater. Sci. Technol.* **2013**, *29* (2), 157−160.

(32) Karuwan, C.; Wisitsorrat, A.; Phokharatkul, D.; Sriprachuabwong, C.; Lomas, T.; Nacapricha, D.; Tuantranont, A. A Disposable Screen Printed Graphene-Carbon Paste Electrode and Its Application in Electrochemical Sensing. *RSC Adv.* **2013**, *3*, 48−55.

(33) Sriprachuabwong, C.; Karuwan, C.; Wisitsorrat, A.; Phokharatkul, D.; Lomas, T.; Sritongkham, P.; Tuantranont, A. Inkjet-Printed Graphene-PEDOT:PSS Modified Screen Printed Carbon Electrode for Biochemical Sensing. *J. Mater. Chem.* **2012**, *2*, 5478−5485.

(34) Liewhiran, C.; Tamaekong, N.; Wisitsora-at, A.; Phanichphant, S. H_2 Sensing Response of Flame-Spray-Made Ru/SnO_2 Thick Films Fabricated from Spin-Coated Nanoparticles. *Sensors* **2009**, *9*, 8996−9010.

(35) Korotcenkov, G.; Boris, I.; Brinzari, V.; Han, S. H.; Cho, B. K. The Role of Doping Effect on the Response of SnO_2-based Thin Film Gas Sensors: Analysis Based on the Results Obtained for Co-Doped SnO_2 Films Deposited by Spray Pyrolysis. *Sens. Actuators, B* **2013**, *182*, 112−124.

(36) Zhang, H.; Feng, J.; Fei, T.; Liu, S.; Zhang, T. SnO_2 Nanoparticles-Reduced Graphene Oxide Nanocomposites for NO_2 Sensing at Low Operating Temperature. *Sens. Actuators, B* **2014**, *190*, 472−478.

(37) Diéguez, A.; Romano-Rodríguez, A.; Vilà, A.; Morante, J. R. The Complete Raman Spectrum of Nanometric SnO_2 Particles. *J. Appl. Phys.* **2001**, *90*, 1550−1557.

(38) Ristic, M.; Ivanda, M.; Popovic, S.; Music, S. Dependence of Nanocrystalline SnO_2 Particle Size on Synthesis Route. *J. Non-Cryst. Solids* **2002**, *303*, 270−280.

DOI: 10.1021/acsami.5b00161
ACS Appl. Mater. Interfaces 2015, 7, 3077−3092

(39) Karelin, A. I.; Leonova, L. S.; Arsatov, A. V.; Dobrovol'skii, Y. A. Vibrational Spectra, Structure and Proton Conduction in Hydrous Tin Dioxide. *Russ. J. Inorg. Chem.* **2013**, *58*, 711−718.
(40) Ni, Z. H.; Wang, Y. Y.; Yu, T.; Shen, Z. X. Raman Spectroscopy and Imaging of Graphene. *Nano Res.* **2008**, *1*, 273−291.
(41) Liu, L.; Zhang, Y.; Wang, G.; Li, S.; Wang, L.; Han, Y.; Jiang, X.; Wei, A. High Toluene Sensing Properties of NiO-SnO_2 Composite Nanofiber Sensors Operating at 330 °C. *Sens. Actuators, B* **2011**, *160*, 448−454.
(42) Zheng, Y.; Wang, J.; Yao, P. Formaldehyde Sensing Properties of Electrospun NiO-Doped SnO_2 Nanofibers. *Sens. Actuators, B* **2011**, *156*, 723−730.
(43) Prieto, P.; Nistor, V.; Nouneh, K.; Oyama, M.; Lefdil, M. A.; Diaz, R. XPS Study of Silver, Nickel and Bimetallic Silver-Nickel Nanoparticles Prepared by Seed-Mediated Growth. *Appl. Surf. Sci.* **2012**, *258*, 8807−8813.
(44) Dupin, J. C.; Gonbeau, D.; Vinatier, P.; Levasseur, A. Systematic XPS Studies of Metal Oxides, Hydroxides and Peroxides. *Phys. Chem. Chem. Phys.* **2000**, *2*, 1319−1324.
(45) Azelee, W.; Bakar, W. A.; Othman, M. Y.; Yong, R. A. C. K.; Toemen, S. The Investigation of Active Sites on Nickel Oxide based Catalysts towards the *in Situ* Reactions of Methanation and Desulfurization. *Mod. Appl. Sci.* **2009**, *3*, 35−43.
(46) Agrawal, A.; Habibi, H. R.; Agrawal, R. K.; Cronin, J. P.; Roberts, D. M. Effect of Deposition Pressure on the Microstructure and Electrochromic Properties of Electron-Beam-Evaporated Nickel Oxide Films. *Thin Solid Films* **1992**, *211*, 239−253.
(47) Zhang, H.; Feng, J.; Fei, T.; Liu, S.; Zhang, T. SnO_2 Nanoparticles-Reduced Graphene Oxide Nanocomposites for NO_2 Sensing at Low Operating Temperature. *Sens. Actuators, B* **2014**, *190*, 472−478.
(48) Liu, S.; Yu, B.; Zhang, H.; Fei, T.; Zhang, T. Enhancing NO_2 Gas Sensing Performances at Room Temperature Based on Reduced Graphene Oxide-ZnO Nanoparticles Hybrids. *Sens. Actuators, B* **2014**, *190*, 472−478.
(49) Kim, B.; Jung, J.; Lee, J.; Kim, J. Precipitate Concentration of Co_2SnO_4 in CoO-Doped SnO_2 Ceramics at Different Oxygen Chemical Potentials. *Solid State Ionics* **2001**, *144*, 321−327.

DOI: 10.1021/acsami.5b00161
ACS Appl. Mater. Interfaces 2015, 7, 3077−3092